Accepted Manuscript

The mechanical and microstructural behaviour of calcite-dolomite composites: An experimental investigation

Alexandra Kushnir, L.A. Kennedy, Santanu Misra, Philip Benson, J.C. White

PII: S0191-8141(14)00292-2

DOI: 10.1016/j.jsg.2014.12.006

Reference: SG 3171

To appear in: *Journal of Structural Geology*

Received Date: 31 March 2014

Revised Date: 4 December 2014

Accepted Date: 14 December 2014

Please cite this article as: Kushnir, A., Kennedy, L.A., Misra, S., Benson, P., White, J.C., The mechanical and microstructural behaviour of calcite-dolomite composites: An experimental investigation, *Journal of Structural Geology* (2015), doi: 10.1016/j.jsg.2014.12.006.

The mechanical and microstructural behaviour of calcite-dolomite composites: An experimental investigation

Authors:

Kushnir, Alexandra[a,1,*]

Kennedy, L.A.[a]

Misra, Santanu[b,2]

Benson, Philip[b,3]

White, J.C.[c]

[a]University of British Columbia, Department of Earth, Oceans, and Atmospheric Sciences, 2020-2207 Main Mall, Vancouver, British Columbia, Canada, V6T 1Z4

[b]Geological Institute, Department of Earth Sciences, Swiss Federal Institute of Technology, Sonneggstrasse 5, Zurich 8092, Switzerland

[c] University of New Brunswick, Department of Earth Sciences, 2 Bailey Dr., Fredericton, New Brunswick, Canada, E3B 5A3

Submitted to the Journal of Structural Geology

Keywords: calcite, dolomite, experiments, shear strain, high temperature, high pressure, grain boundary sliding, fracture, strain partitioning

*Corresponding author: Email address: alexandra.kushnir@gmail.com (Alexandra Kushnir)

[1] Institut des Sciences de la Terre d'Orléans, UMR 7327 – CNRS/Université d'Orléans, 1A, Rue de la Férollerie, 45071 Orléans Cedex 2, France

[2] GNS Science, 1 Fairway Drive, Avalon 5010, Wellington, New Zealand

[3] Rock Mechanics Laboratory, School of Earth and Environmental Sciences, Burnaby Building, University of Portsmouth, PO1 3QL, United Kingdom

Abstract

The styles and mechanisms of deformation associated with many variably dolomitized limestone shear systems are strongly controlled by strain partitioning between dolomite and calcite. Here, we present experimental results from the deformation of four composite materials designed to address the role of dolomite on the strength of limestone. Composites were synthesized by hot isostatic pressing mixtures of dolomite (Dm) and calcite powders (% Dm: 25%-Dm, 35%-Dm, 51%-Dm, and 75%-Dm). In all composites, calcite is finer grained than dolomite. The synthesized materials were deformed in torsion at constant strain rate ($3x10^{-4}$ and $1x\ 10^{-4}\ s^{-1}$), high effective pressure (262 MPa), and high temperature (750°C) to variable finite shear strains. Mechanical data show an increase in yield strength with increasing dolomite content. Composites with <75% dolomite (the remaining being calcite), accommodate significant shear strain at much lower shear stresses than pure dolomite but have significantly higher yield strengths than anticipated for 100% calcite. The microstructure of the fine-grained calcite suggests grain boundary sliding, accommodated by diffusion creep and dislocation glide. At low dolomite concentrations (i.e. 25%), the presence of coarse-grained dolomite in a micritic calcite matrix has a profound effect on the strength of composite materials as dolomite grains inhibit the superplastic flow of calcite aggregates. In high (>50%) dolomite contents samples, the addition of 25% fine-grained calcite significantly weakens dolomite, such that strain can be partially localized along narrow ribbons of fine-grained calcite. Deformation of dolomite grains by Mode I cracks and shear fractures is observed; there is no intracrystalline deformation in dolomite irrespective of its relative abundance and finite shear strain.

1. Introduction

The styles and mechanisms of deformation associated with many variably dolomitized limestone shear systems are strongly controlled by strain partitioning between dolomite and calcite. Furthermore, the mechanical behaviour of shear zones that form in calcite-dolomite composites is likely a function of external parameters (e.g. P_c,P_p, T, and $\dot{\gamma}$), the mineralogy (calcite/dolomite content; (Delle Piane et al., 2009a)), and texture (e.g. grain size and porosity) of the rock. Carbonate fault rocks can have heterogeneous distributions and variable contents of calcite and dolomite. For instance, fluid flow during thrusting can result in partial de-dolomitization (i.e. calcite formation) of carbonates resulting in heterogeneous distribution of calcite and dolomite in fault rocks (Erikson, 1994). Conversely, shear strain, in tandem with fluid flow, may result in a more dolomite-rich fault rock than the protolith due to the dissolution of calcite and subsequent passive enrichment of dolomite along thrust faults (Kennedy and Logan, 1997). Fault rocks derived from carbonate rocks can therefore be composed of variable amounts of dolomite and calcite and grain sizes distributions within the fault rocks can be heterogeneous. In many shear zones, dolomite is demonstrably stronger than calcite, but the amount of dolomite required to significantly change the rheological behaviour of carbonate shear zones is poorly understood. Field observations suggest that dolomite may lead to the embrittlement of limestone (Viola et al., 2006). However, despite the common occurrence of limestone-dolomite composites, the influence of dolomite content on the strength of limestone under both ambient and high temperature conditions is poorly understood.

The deformation response of pure calcite and, to a lesser extent, pure dolomite under a variety of crustal conditions is well understood. Field observations suggest that under similar conditions of deformation, below amphibolite facies metamorphism, dolomitic rocks are stronger than limestone of similar grain size and porosity. During deformation, dolomite generally becomes highly fractured whereas calcite undergoes dislocation creep and dynamic recrystallization (Bestmann et al., 2000; Erikson, 1994; Woodward et al., 1988). Under similar experimental deformation conditions, dolomite rock is stronger and less ductile than limestone (Davis et al., 2008; Griggs et al., 1951, 1953; Handin and Fairburn, 1955; Higgs and Handin, 1959; Holyoke et al., 2013). At high temperatures (> 700°C), coarse grained dolomite is still stronger than calcite; however, fine-grained dolomite rocks (grains less than 15 μm in diameter) weaken significantly and can be weaker than calcite-rich rocks deformed under the same conditions (Davis et al., 2008; Delle Piane et al., 2009a; Delle Piane et al., 2008; Holyoke et al., 2013).

In this study, we address the role of coarse-grained dolomite on the strength and microstructural evolution of calcite-dolomite composites. Synthetic, hot isostatically pressed (HIP) calcite-dolomite (Cc-Dm) composites of four unique compositions - 1) 25%Dm:75%Cc, 2) 35%Dm:65%Cc, 3) 51%Dm:49%Cc, 4) 75%Dm:25%Cc (hereafter designated by their dolomite content (%): Dm25, Dm35, Dm51, and Dm75) - were deformed in a torsion apparatus at elevated temperature and confining pressure to determine their rheological behaviour and to evaluate the effect of dolomite content and grain size on rock strength. A total of 13 rock deformation experiments were conducted at the following conditions: temperature (T) of 750°, effective pressure (P_{eff}) of 262 MPa, imposed maximum shear strain rates ($\dot{\gamma}$) of $1x10^{-4}$ s^{-1} and $3x10^{-4}$ s^{-1}, and total shear strains (γ) between 0.16 and 5.5. We observe that 1) in carbonate composites, even low dolomite contents greatly affect rock strength; 2) coarse-grained dolomite accommodates strain by brittle deformation in high dolomite content samples; and 3) calcite deforms by dislocation glide and diffusion creep assisted grain boundary sliding. Finally, we compare the experimental results to other studies and comment on their application to natural deformation environments.

2. Starting Material

2.1. Starting Powders and Sample Preparation

Two end member powders (coarse-grained dolomite and fine-grained calcite; described below) were mixed in varying proportions to produce four distinct compositions: Dm25, Dm35, Dm51, and Dm75.

Reagent-grade calcite powder (Minema 1™) was supplied by Alberto Luisoni AG, Mineral- & Kunststuffe and is characterized by equiaxed calcite grains exhibiting rare growth twins. The powder has a modal grain size of 9 μm (Figure 1A), as measured with a Mastersizer 2000 laser diffraction particle size analyser (Malvern Instruments Ltd.;). Rietveld refinement of XRD spectra (Raudsepp et al., 1999) of the calcite powder confirms its composition to be 99% $CaCO_3$; the remaining constituents are Mg, Al, Fe, and Si oxides.

A 4 kg block of Badshot marble, a natural dolomite marble from the Selkirk Mountains of British Columbia, was crushed to produce a powder with a broad grain size distribution and modal grain size of ~120 μm (Figure 1A). Badshot dolomite is characterized by coarse dolomite grains (mean grain size of 477 μm, Austin and Kennedy (2005)) featuring lobate grain boundaries and fine, polygonal grains. Cleavage and twinning are prevalent in most grains

(Austin, 2003; Austin and Kennedy, 2005; Austin et al., 2005). XRD analysis of the powder indicates a mineralogy that is ~99.8% dolomite. Thin section analysis reveals trace quantities (<< 1%) of pyrite, apatite, calcite, tremolite, and white mica; these accessory phases are sufficiently low in abundance to be undetected by XRD analysis.

The powder mixtures were mechanically shaken to create homogeneous mixtures; the grain size distributions of the mixed powders are shown in Figure 1B. The starting powders have a bimodal grain size distribution, reflecting the dolomite proportion. The powder mixtures were then dried at 120°C for a minimum of 24 hours before being cold pressed into stainless steel, cylindrical canisters. The canisters were filled and pressed in 20g increments to produce homogenous packing of the powder along the canister length. This was done to avoid pressure shadow development during heat treatment. Pressing was done with an Enerpac-H-Frame 50 ton press up to a load of 40 tons, corresponding to a vertical stress of 200 MPa. A small volume of alumina powder with a porosity of ~30% was placed at the top and bottom of the canisters to act as a CO_2 sink for decarbonating dolomite. This ensured the migration of the emitted CO_2 to the storage areas, allowing the porosity to remain reduced in the rest of the canister.

All canisters were welded shut and, subsequently, hot isostatic pressed (HIP) to produce synthetic composite rock samples. The HIP was performed in a large volume, internally heated, argon gas apparatus at ETH-Zürich under a confining pressure of 170 MPa (Delle Piane et al., 2009a) and a temperature of 700°C for 4 hours. The resulting products form a suite of coherent, sintered material of known compositions and consistent grain size. Rietveld refinements of XRD spectra collected on the composite samples did not detect periclase (MgO) nor lime (CaO), indicating that there was no detectable decarbonation of dolomite or calcite during the HIP process. Rietveld refinements also confirm the four starting material compositions as containing 25%, 35%, 51%, and 75% dolomite.

2.2. Microstructural and Textural Analyses

Starting materials were thin sectioned normal to the canister long axes (i.e. normal to the pressing direction) and polished using a rotary polishing wheel and 200 nm silica bead colloidal solution. Backscatter electron (BSE) and secondary electron (SE) SEM images were collected using a thermal field emission type Zeiss Sigma SEM (UBC) with 1.3 nm resolution at 20 kV acceleration voltage. Probe current was 1.37 nA.

Electron Backscatter Diffraction (EBSD) analysis was completed to map the crystallographic preferred orientation (CPO) of the starting materials and the evolution of the

CPO of subsequently deformed materials. EBSD measurements were made using an EDAX DigiView EBSD camera (UBC). Samples were inclined to the electron beam at 70° to produce clear diffraction patterns for automated identification using Orientation Imaging Microscopy (OIM™) Data Collection and Data Analysis software. The average crystallographic orientation for each individual grain was used to generate pole figures using PF_Euler_PC.exe (Pera et al., 2003). CPO strength is characterized by the J-texture index (the density distribution of the crystallographic orientations (Miyazaki et al., 2013)); we use both the pole figure J-index (pfJ) and the J-index (J). Indices vary from 1 (random crystallographic orientations; no CPO) to infinity (one discreet crystallographic orientation). The J-index (calculated using mtex-3.5.0 (Bachmann F., 2010)) incorporates all slip systems, while the pfJ-index (calculated using PF_Euler_PC.exe) is a measure of the strength of the CPO along a defined slip axis (i.e. c-axis).

Energy-dispersive X-ray spectroscopy (EDS) was performed on all analyzed samples using an Apollo XL Silicon Drift Detector (SDD) at a typical working distance of 14 mm. EDS data were collected in conjunction with EBSD diffraction patterns and used to identify dolomite based on the apparent relative concentrations of Mg:Ca. EDS spectra suggesting Ca:Mg ratios ~1 were interpreted as indicating the presence of dolomite.

2.3. Starting Material Characterization

The skeletal and isolated pore space volume, V_{s+i}, of each sample was determined prior to deformation using a Micrometritics Multivolume Pycnometer 1305 helium pycnometer. Connected porosity, ϕ, was calculated from the geometric bulk volume, V_b, and skeletal and isolated pore volume:

$$\phi = \left(1 - \frac{V_{s+i}}{V_b}\right) \times 100\% \qquad (1)$$

The final composition, porosity, and density of the starting materials are given in Table 1.

Calcite grains are approximately equiaxed, generally have straight grain boundaries, and are closely packed with triple junction grain boundaries (Figure 2A and 2C). Porosity is isolated along grain boundaries and at triple junctions and therefore may not be accessed by the helium gas pycnometer; the porosity data obtained by pycnometry are considered lower limits.

Dolomite grains are generally distributed homogeneously in all synthetic starting materials (Figures 2B and 2D); rarely, coarser grains of dolomite may cluster together. Dolomite grains are angular to subangular and contain intragranular fractures; straight fractures appear to follow cleavage planes but curved fractures also exist. Since these fractures do not continue into

the calcite matrix, they are attributed to the crushing process used to produce the starting dolomite powder. Intergranular porosity is greatest at dolomite-calcite interfaces (Figure 2C).

Observations of the Dm25 and Dm35 starting materials made by SEM reveal randomly distributed circular concentrations of calcite up to ~500 μm in diameter (Figure 3A). These concentrations are spherical and likely accreted during mechanical shaking of the starting powders. The margins of these calcite aggregates are accentuated by concentrations of edge-parallel oriented dolomite grains (Figure 3B). Similarly, coarse dolomite grains can also be encased in a halo of predominantly fine-grained calcite.

Individual calcite grains within the starting materials are undeformed, showing little to no undulose extinction. Lower hemisphere stereographic projections for calcite obtained from EBSD analysis indicate a weak CPO of the calcite c-axis (Figure 2B and 2D). The c-axis is oriented perpendicular to the load direction during cold pressing as observed by Rutter et al. (1994b), and regardless of calcite content does not vary significantly. Dolomite in the starting materials shows no CPO along any of the common dolomite glide planes (Figures 2B and 2D). The CPO peaks on the dolomite stereonets are artefacts caused by the relatively small number of dolomite grains in the scanned area (a result of their large grain size) and cause erroneously high pfJ-indices, indicating strong textures focused around single grains.

Grain size distributions based on two-dimensional images for Dm25 and Dm75 were calculated using Orientation Imaging Microscopy (OIM™) data analysis software by fitting a model ellipse to each crystallographically identified grain (Figure 4). Both starting compositions show similar calcite grain size distributions; Dm25 and Dm75 have modal calcite grain sizes of 5.5 μm and 4.5 μm, respectively (Figure 4A). Dolomite grain size distributions are shown in Figure 4B. These estimates are less precise than for calcite because there are fewer dolomite grains in the scan areas, but we observe a broad grain size distribution ranging between 0 and 100 μm.

3.0. Deformation Apparatus and Techniques

The HIP material was cored into 10 mm and 15 mm diameter cylinders. The core ends were flattened and polished perpendicular to the cylinder sides. Samples were dried in an oven at 100°C then mounted between alumina and partially stabilized zirconia spacers and encased in iron jacketing. A jacket thickness of 0.25 mm was used for 15 mm diameter samples. Jackets for

10 mm diameter samples were swaged to the correct inner diameter resulting in thickening of the jacket wall to 0.4 mm.

All experiments were performed using an internally heated, argon-confining medium pressure vessel equipped with torsion actuator, described by Paterson and Olgaard (2000) (Figure 5A). The experiments were performed in torsion at constant angular displacement rates, corresponding to constant maximum shear strain rates of $1x10^{-4}$ s^{-1} and $3x10^{-4}$ s^{-1}. Confining pressure and temperature were held constant at 300 MPa and 750°C, respectively. Sample temperature was monitored using a K-type thermocouple placed 3mm above the sample. The thermal profile along the sample was calibrated to be consistent within 1°C. All samples were heated and cooled at 10°C/min.

The applied torque was measured using an internal load cell equipped with a pair of pre-calibrated linear variable differential transformers (LVDTs). Measured torque was corrected for the strength of the iron jacket (Barnhoorn, 2003) and converted to shear stress at the sample surface:

$$\tau = \frac{4\left(3+\frac{1}{n}\right)M}{\pi d^3} \qquad (2)$$

where τ is shear stress, *M* is internal torque, *d* is the diameter of the sample, and *n* is the stress exponent (Paterson and Olgaard, 2000). In this study, the power law creep relationship used is:

$$\dot{\gamma} = A\tau^n e^{\frac{-Q}{RT}} \qquad (3)$$

where *A* and *Q* are constants, *n* is the stress exponent, *T* is the temperature, and *R* is the gas constant (Paterson and Olgaard, 2000). *n* is experimentally determined for a given composition by conducting a strain rate stepping experiment and plotting the total torque response (*M*) to changing strain rate ($\dot{\gamma}$). As *M* is linearly related to τ, the slope of the log-log plot $\dot{\gamma}$ vs. *M* yields *n* according to:

$$n = \frac{d\ln\dot{\gamma}}{d\ln M} \qquad (4)$$

Comparison between torsion and axial experiments is necessary for comparing our data to studies of other carbonate systems. At the same nominal strain rates ($\dot{\varepsilon} = \dot{\gamma}$), differential stress ($\sigma_1 - \sigma_3$) is calculated:

$$\sigma_1 - \sigma_3 = 3^{\frac{1+n}{2n}}\tau \qquad (5)$$

where σ_1 is the calculated maximum compressive stress, σ_3 is the minimum compressive stress, and τ is shear stress (Paterson and Olgaard, 2000).

4.0. Mechanical Results

To maintain the stability of dolomite, we performed all experiments under unvented conditions and within the stability field of calcite and dolomite (Goldsmith, 1959). XRD analysis revealed no evidence of decarbonation products; we conclude that the low porosity of our starting materials allowed equilibrium pore pressures to be reached by the dissociation of trace amounts of dolomite (Davis et al., 2008; Delle Piane et al., 2009a; Holyoke et al., 2013). We have accounted for the effective pressure caused by the decarbonation of trace amounts of dolomite, such that $P_{eff}=P_C-P_{CO2}$.

All experiments performed in this study, including experimental conditions and sample compositions, are summarized in Table 2. Dm25, Dm35, and Dm75 samples were deformed in strain rate stepping experiments to empirically determine the stress exponent *n* (see Table 2, Figure 6). All mechanical data are fit using Eq. (2) and are shown in Figure 7A (high strain rate experiments) and Figure 7B (low strain rate experiments). High strain rate ($\dot{\gamma} = 3 \times 10^{-4} s^{-1}$) experiments were conducted for all four compositions (experiments P1522, P1524, P1525, P1527, P1528, P1537, and P1538) at T=750°C and P_c=300 MPa. The shear strain for these experiments exceeded $\gamma = 5$ (Figure 7A). Experiment P1537's (Dm51) heating history is not confidently known beyond $\gamma \sim 2$; only the mechanical data up until this point is used and this sample was not used for microstructural analysis. Low strain rate ($\dot{\gamma} = 1 \times 10^{-4} s^{-1}$) experiments were conducted for compositions Dm35 (P1543), Dm51 (P1523), and Dm75 (P1533) at T=750°C and P_c=300 MPa (Figure 7B). The maximum shear strain for these experiments was approximately $\gamma \sim 2$.

Yield and peak strength of the synthetic composite samples increases with increasing dolomite content (Table 2; Figure 7C). Yield strength was taken as the departure from the elastic response of the material. Experiments P1527 (Dm25) and P1524 (Dm35) are mechanically similar, both reaching a peak strength of ~80 MPa (Figure 7A). Mechanical steady-state (~79 MPa) is established in both samples at $\gamma < 0.1$ followed by limited strain hardening in Dm25 at $\gamma \sim 3.75$ (Figure 7A). Experiments P1525 and P1528 (Figure 7A) failed due to jacket ruptures resulting from the inherent strength of the Dm51 and Dm75 materials at 15 mm sample diameters. To mitigate this behaviour, Dm51 (P1537) and Dm75 (P1538) sample diameters were reduced to 10 mm so that these compositions could be deformed to high strain. P1537 (Dm51) reached a tenuous steady-state at $\tau \sim 140$ MPa and $\gamma \sim 0.4$ (Figure 7A). The mechanical behaviour of the Dm75 sample evolves throughout deformation: after attaining a peak strength of ~178

MPa, dramatic strain weakening at $\gamma \sim 1$ is recorded (Figure 7A). Strain hardening and subsequent strain weakening are observed between $3 < \gamma < 4$. Experiments P1533 and P1543 were halted manually.

5. Microstructure and Texture of Deformed Materials

5.1 Analytical Methods

After deformation, all samples were cut along the longitudinal tangential section of the core (Figure 5B) and doubly-polished petrographic thin sections were prepared with Crystalbond© adhesive. This plane shows the maximum shear strain attained in the sample.

In addition to SEM, EBSD, and EDS analyses (see Section 2.2.), microstructures for transmission electron microscopy (TEM) were selected. After having been mounted on 3mm copper discs, the areas were thinned by Ar-ion bombardment in a Gatan PIPS thinning unit. TEM examination was performed with a JEOL 2011 STEM apparatus operated at 200kcV.

Electron-probe micro-analyses of selected deformed samples were done to confirm exact grain composition. Data were collected on a CAMECA SX-50 instrument, operating in the wavelength-dispersion mode using: excitation voltage: 15 kV; beam current: 10 nA; peak count time: 20 s; background count-time: 10 s; spot diameter: 10 μm. Data reduction was done using the 'PAP' $\phi(\rho Z)$ method (Pouchou and Pichoir, 1985).

5.2 Microstructure: low dolomite content samples

The circular calcite aggregates identified in starting materials Dm25 and Dm35 (Figure 3) are deformed non-coaxially into thin bands (ellipsoids) of pure calcite with aspect ratios ranging from 19 to 23 (Figure 8A). These thin layers of pure calcite, interlaced with the calcite-dolomite mixture, define a compositional layering in the low dolomite content samples (Dm25 and Dm35; Figures 8A and 8B). As these aggregates were originally circular in cross-section and assuming there was no loss of volume during deformation, the shear strain by simple shear can be calculated:

$$\gamma = \cot \alpha' - \cot \alpha \qquad (6)$$

where α is the initial angle between a line and the direction of shear, and α' is the same angle after deformation. For the torsional simple shear assumption, the instantaneous stretching axis is oriented in the xz-plane at 45° to the direction of shear and is equal to α for the initially circular aggregates. Accumulation of strain with increasing imposed sample twist produces the maximum

stretching direction preserved by the long axis of the elliptical calcite aggregates. The angle between this orientation and the direction of shear is α' (Figure 8A). These features record shear strains of 5.14 and 6.11 for Dm25 and Dm35, respectively.

Calcite layers are sheared and rotated nearly parallel to the shear direction, while the surrounding dolomite-calcite mixture defines a shape foliation oblique to the shear direction (Figure 8B), defining a global s-c mylonite fabric. Dolomite grains with high aspect ratios (i.e. aspect ratios > 1) are subject to rigid body rotation and their long axes are aligned subparallel to the layering, inclined to the shear direction; these are interpreted as shape (s-) fabrics (Figures 8B and 8C). Accessory pyrite is elongated and passively marks the local fabric (Figure 8C) while thin, discontinuous zones of relative high shear strain are oriented nearly parallel to the shear direction and are interpreted as c-surfaces (Figure 8D).

Calcite grains are generally polygonal, equiaxed to tabular, and closely packed with straight grain boundaries meeting at triple junctions (Figure 8E). The more tabular shaped calcite grains are aligned parallel to the shape foliation (inclined to the shear direction; Figure 8E). Calcite grains comprising the pure calcite layers are also mostly equiaxed, with straight grain boundaries exhibiting triple junctions. Two dimensional grain size distributions for Dm25 show possible calcite grain growth during deformation from 6 μm to 7.5 μm (Figure 4A). The dolomite grains show little to no evidence of internal strain nor is there any evidence of grain size reduction due to fracture (Figures 8A and 8C). Dolomite grains do not appear to have sustained any additional fracture (e.g. microcracking and shear fracturing), as fracture density is qualitatively the same as in the starting material. Rounding of dolomite grains less than approximately 50 μm in diameter is observed in all dolomite-poor deformed samples. While dolomite grains <100 μm show some rounding (Figure 8B and 8E), there is no significant rounding of grains above ~100 μm.

Porosity is visibly reduced with respect to the starting material and is typically preserved at triple junctions of calcite grains (Figure 8E). Locally, there are regions of higher porosity within the calcite matrix aligned along foliation (Figure 8F). These regions are located in pressure shadow-like geometries along the peripheries of some dolomite grains that are > 70 μm in diameter (Figure 8F).

5.3 Microstructure: High dolomite content samples

In high dolomite content (>50%) samples, a poorly developed compositional layering is defined by crude variations in grain size and fine-grained, high aspect ratio dolomite (Figure 9A

and 9B). Locally, a shape fabric inclined to the shear direction is defined by rotated dolomite grains <20 μm in diameter (Figure 9B). Areas of localized strain in the patchy calcite layers are common. Thin, interconnected networks of fine-grained calcite form ribbons that define a discontinuous and irregular foliation that is deflected around more rigid coarse-grained dolomite (Figure 9A and 9C). Sheared pyrite grains wrap around dolomite grains (Figure 9A and C).

The calcite microstructure is similar to the low dolomite samples; calcite grains are locally equiaxed to tabular, bounded by straight grain boundaries, and form triple junctions with neighbouring calcite grains (Figure 9B). In areas of high dolomite content, irrespective of the overall shape fabric, calcite grain are oriented parallel to the dolomite grain boundaries (especially in narrow regions between dolomite grains; Figure 9B). Two dimensional grain size distributions for P1538 (Dm75) show possible calcite grain size reduction during deformation (from 4.5 to 3.5 μm) in Dm75 (Figure 4A).

Brittle deformation of dolomite is evident in all high dolomite content samples: intragranular Mode I fractures are common in the larger dolomite grains and are lined with fine grained calcite (Figure 9A). These fractures do not propagate into the surrounding calcite matrix. Locally, dolomite is fragmented by domino-style and antithetic shear fractures (Figure 9A and 9D).

5.4 Deformation Textures

EBSD analyses of samples Dm25, Dm35, and Dm75 taken to high strain show a strong crystallographic preferred orientation of calcite crystals (Figure 10). The c-axes define double maxima with the bisecting line normal to the direction of maximum stretching, indicating basal slip activation. With increasing dolomite content, the c-axis CPOs become more diffuse, though pfJ- and J-indices are comparable (Figure 10B vs. 10E). In all cases, the c-axis patterns are most pronounced, followed by the a-axis system. As in the c-axis system, the a-axis girdles are well defined but are symmetric about the direction of shear. While a dominant CPO is observed, calcite grains appear internally strain free, showing little to no evidence for significant internal strain (indicated in the EBSD maps by uniform grain crystal lattices). However, preliminary TEM observations (Figures 11A and 11B) show that, despite the EBSD observations, dislocations are common while subgrains are absent.

The spherical calcite aggregates (observed in the starting material, Figure 3) that deformed to ellipses during shear (Figure 8A) have the strongest crystallographic preferred orientations. Figure 12 is a compilation of four EBSD scans across a sheared calcite layer from

the dolomite-calcite matrix into the calcite layer. It highlights the effect of the second phase (dolomite) on calcite fabric development. The calcite layer has higher pfJ- and J-indices (Figure 12E), indicating a stronger texture than the surrounding calcite-dolomite matrix (Figure 12B, 12C, and 12C). The CPO of a region scanned ~600 μm away from the calcite layer (Figure 12C) shows the 'background' CPO of the matrix: both the c and a axes are well defined and asymmetrically distributed around the SZB and normal to the SZB, respectively. Adjacent to the calcite layer (~100 μm away from the calcite band; Figure 12D), which still contains dolomite grains, calcite has a similar CPO to that shown in Figure 12C. Within the calcite layer (Figure 12E), the CPOs show the tightest clusters. The c-axis is symmetrically distributed perpendicular to the shear zone boundary (SZB).

To illustrate the evolution of fabric with increasing shear strain, thin sections were cut from different longitudinal axial sections (see Figure 5B) from the same core for each experiment, and CPOs were measured using EBSD (Figure 13). The calcite c-axes are inclined to the shear zone boundary and define tighter maxima with increasing shear strain. The pfJ- and J-indices also increase with increasing strain. For the Dm75 experiment, the c-axis maxima are more diffuse than for the Dm25 and Dm35 experiments.

There is no well-developed CPO in dolomite from deformed samples (Figure 10C and 10F), nor is there pervasive undulose extinction, though Dm75 shows minor undulose extinction in coarse-grained dolomite. The pfJ- and J-indices do not vary significantly from the starting material, although they are higher than the same indices for calcite. We interpret this to be, in large part, due to the limited number of data points used to calculate these values.

6. Chemical Changes Attending Deformation

EDS analysis of calcite and dolomite grains in deformed samples highlights changes in composition with increasing shear strain. In particular, the magnesium contents of calcite grains increase with increasing strain. This is most pronounced in calcite grains proximal to fine-grained dolomite phases. Figure 14 demonstrates the evolution of magnesium transfer from $\gamma=0$ (Figure 14A) to the largest strains (Figure 14C) for P1527 (Dm25). At $\gamma=0$, magnesium is restricted to dolomite grains, but with increasing strain magnesium becomes more mobile and defines a foliation between dolomite grains (white streaks in Figure 14C).

Electron microprobe analysis was used to quantify the extent of Mg^{2+} migration from dolomite to calcite during deformation in high strain experiments P1527 (Dm25) and P1538

399 (Dm75). Microprobe analysis confirms depletion of Mg^{2+} in fine-grained dolomite proximal to
400 Mg^{2+} enriched calcite in Dm25; however, calcite removed from dolomite grain boundaries is not
401 enriched. Mg-enrichment of calcite is pervasive in Dm75, regardless of proximity to thin ribbons
402 of plastically deformed calcite, owing to the abundance of dolomite throughout the system.
403 Microprobe data can be found in the Supplementary Materials.

404 **7. Discussion**

405 *7.1. The Role of Dolomite*

406 In all our experiments, peak shear stress is higher than that determined for 100% calcite
407 of the same grain size and deformed under similar experimental conditions (Figure 7C). For
408 example, the peak shear stress for pure, synthetic calcite aggregates with an average grain size of
409 7 μm deformed in torsion at 727°C, P_c = 300 MPa, and $\dot{\gamma} = 3x10^{-4}$ s^{-1} is 15 MPa (Barnhoorn et
410 al., 2005a). Peak shear stresses for Solnhofen limestone (grain size ~5 μm) under the same
411 conditions were ~40 MPa (Barnhoorn et al., 2005a). Predicted equivalent shear flow stresses for
412 diffusion creep in Mg-rich calcite (Herwegh et al., 2003) and pure calcite (Walker et al., 1990)
413 are 6 MPa and 13 MPa, respectively (see Herwegh et al. (2005) for flow law parameters used).
414 All these peak stresses are significantly lower than the peak shear stress attained during the
415 Dm25 dolomite content experiments (79 MPa for P1522 and 82 MPa for P1527) in this study.
416 These larger recorded shear stresses may be symptomatic of an increased strain rate in the calcite
417 phase as it deforms around rigid dolomite. Indeed, assuming all deformation in our samples is
418 accommodated within the calcite phase, the predicted shear strain rates calculated using the peak
419 shear stresses recorded for P1527 (Dm25) are over one order of magnitude faster ($6x10^{-3}$ s^{-1} and
420 $4x10^{-3}$ s^{-1} for pure and Mg-rich calcite, respectively; see Herwegh et al. (2005) for flow laws and
421 flow law parameters used) than the imposed strain rate of $3x10^{-4}$ s^{-1}.

422 In our low-dolomite content experiments (Dm25 and Dm35), coarse-grained dolomite
423 grains show no evidence of extensive brittle or intracrystalline deformation. However, finer
424 grained dolomite (< 50 μm) with aspect ratios >1 are rotated into the foliation, suggesting their
425 active role as rotating rigid bodies. We propose that most shear strain was partitioned into the
426 fine-grained calcite layers and that although the dolomite grains are not internally strained or
427 highly fractured, the distribution of these rigid bodies acts to create anastomosing, connected
428 networks of calcite grains. In effect, the dispersed dolomite grains provide local resistance to
429 grain boundary sliding and this resistance results in an increase in the flow stresses necessary for
430 steady state deformation.

Although we observe a moderate increase in strength in the 51% dolomite experiment relative to Dm25 and Dm35 (Figure 7A), the Dm75 sample shows a two-fold increase in strength over compositions Dm25 (P1522 and P1527) and Dm35 (P1524). We interpret the high yield stress of Dm75 as a result of the load being supported by dolomite-dolomite contacts. We propose that the significant shear stress drop in experiment P1538 (Dm75) represents fracture of dolomite grains by Mode I, shear fractures, and subsequent grain size reduction (refer to Figures 9A and 9D). A short-lived steady state is attained once a temporary grain boundary network is established within the fine-grained calcite (Figure 9C), permitting grain boundary sliding. In essence, disruption of the calcite network leads to strain hardening while re-establishment of the calcite networks leads to the final strain weakening (Figure 7A). Similar behaviour is suggested for the strong phases in other multi-phase systems (e.g. Rybacki et al. (2003)). For instance, in quartz-calcite composites, the addition of quartz (the strong phase, analogous to dolomite in our system) significantly increases the flow stress needed for steady state deformation (Rybacki et al., 2003).

In our experiments, the high dolomite content (75%) samples are strongest, yet they are significantly weaker than 100% coarse- grained dolomite deformed under similar elevated pressure-temperature conditions (Figure 7C; (Davis et al., 2008; Holyoke et al., 2013). The peak shear stress of 167 MPa achieved in experiment P1538 (Dm75) is lower than the reported strengths for Madoc dolomite (grain size of 240 μm) at 700°C (equivalent yield shear stress of 241 MPa; equivalent shear stress at 5% strain of 377 MPa; equivalent $\dot{\gamma} = 2x10^{-4}$ s^{-1}) and 800°C (equivalent peak shear stress of 257 MPa for an equivalent $\dot{\gamma} = 1.7x10^{-5}$ s^{-1}). We attribute the relative weakness in our Dm75 sample to the role of calcite networks in weakening the rocks. Coarse-grained dolomite does not undergo any significant intracrystalline plasticity and deforms, instead, by fracture. We interpret that shear strain is partitioned into thin, fine-grained, interconnected calcite-dolomite layers that are developed during shear strain and are deflected around large dolomite clasts (Figure 9C). This shear strain-induced configuration results in a weaker rock.

Our data suggest that for dolomite contents below a minimum of 35%, dolomite does not actively deform, but its presence is rate-controlling given the strength of the composites compared to micritic limestone (Figures 7C and 15A). Only when dolomite, the ‘strong’ phase, is present in sufficient quantities (>51%) to inhibit the flow of calcite and/or restrict calcite flow to narrow, localized bands does brittle fracture of dolomite grains become mechanically

463 significant in accommodating strain, indeed, leading to the initial embrittlement within the
464 system.

465 We propose that in shear systems containing <75% dolomite (with the remaining being
466 calcite), rocks will have the ability to accommodate significant shear strain at much lower shear
467 stresses than dolomite. Conversely, even at low concentrations (i.e. 25%), the presence of
468 coarse-grained dolomite in a micritic calcite matrix will have a profound effect on the strength of
469 composite materials; the strength increases with respect to a pure calcite system since dolomite
470 grains inhibit the superplastic flow of calcite. Eventual embrittlement of dolomite within the
471 system may be required to re-establish plastic networks of fine-grained calcite.
472

473 *7.2 The Case for Grain Boundary Sliding*

474 Contrasting stress exponents determined from the strain rate stepping experiments of
475 Dm25, Dm35, and Dm75 suggest the influence of more than one deformation mechanism. For
476 the adopted relationship, $\dot{\gamma} \propto \tau^n$, calcite-rich samples give n = 1.7±0.23 (Dm35; P1529) and
477 2.0±0.43 (Dm25; P1711), while dolomite-rich samples give n = 3.6±0.12 (Dm75; P1713).
478 Broadly interpreted, a $n \geq 3$ reflects dislocation creep related flow (Weertman, 1957), while
479 $1 < n < 3$ correlates with a grain-size-sensitive (GSS) rheology (Schmid et al., 1977). GSS
480 deformation involves a component of independent grain boundary sliding that is accommodated
481 by grain boundary diffusion (n = 1; Coble (1963)) or grain boundary dislocations (n = 2, Gifkins
482 (1976)).

483 In this study, the n = 1.7 and 2.0 determined for low dolomite experiments (Dm25 and
484 Dm35) suggest a component of GSS rheology. The low dolomite composites attain mechanical
485 steady state immediately following yield shear stress, which suggests the development of a stable
486 microstructure. Microstructurally, the calcite matrices comprise small, equidimensional,
487 polygonal grains that are strain free at the optical microscope and EBSD scale: a microstructure
488 typically associated with GSS creep (Rutter, 1974; Schmid, 1976; Schmid et al., 1977; Walker et
489 al., 1990). In addition, we do not observe any subgrains and there is no evidence for dynamic
490 recrystallization. Furthermore, grain size distributions of the starting and deformed materials
491 show limited change in calcite grain size; the grain size data calculated from EBSD processes
492 record neither significant grain growth nor grain size reduction in the deformed samples.

493 Preliminary TEM observations of the calcite aggregates show that dislocations are
494 abundant while subgrains are absent (Figure 11). The dislocation density and the absence of

subgrains in tandem with polygonal grains meeting at triple junctions are consistent with shear strain accommodated by independent grain boundary displacements (Langdon, 2006). Reconciliation of the experimental and textural data is accomplished by considering mixed-mode deformation of the calcite aggregates including: independent grain boundary sliding, intracrystalline dislocation glide, and diffusion creep (Casey et al., 1997). This behaviour is characterized by near Newtonian flow ($n = 1$; typically $1 < n < 3$ for constitutive equations of the form $\dot{\gamma} \propto \tau^n$) and is observed for temperatures >0.5 the material's homologous temperature (Langdon, 2006). We expect grains to be equiaxed, polygonal, strain free, and generally less than 10 microns in diameter. As a result of irregularities at grain boundaries and, especially, at the junctions where more than two grains meet, independent grain boundary sliding is accomplished by Rachinger sliding resulting in strain free, equiaxed grains. Grain boundary sliding also encourages chemical exchange between phases, such as the transfer of Mg^{2+} between phases observed in our experimental run-products, since neighbouring grains are constantly moving past one another (Herwegh et al., 2003).

Critically, small quantities of Mg^{2+} in calcite limit grain growth, thereby keeping grain size sensitive diffusion creep and grain boundary sliding operative during deformation (Herwegh et al. (2003), even under high homologous conditions. Herwegh et al. (2003) found that calcite grain size is inversely proportional to Mg-content, resulting in an extrinsic control on strength as calcite grain growth is inhibited. In our experiments, Mg^{2+} migration from dolomite to calcite confirms that diffusion creep processes occurred during deformation. Diffusion processes likely contributed to maintaining the small calcite grain size throughout the experiments (Davis et al., 2008; Delle Piane et al., 2009a; Delle Piane et al., 2008; Holyoke et al., 2013). Rybacki et al. (2003) suggest that in the quartz-calcite system, Si incorporated into the dislocation cores of calcite is responsible for the increase in flow strength of calcite. It is unknown if a similar driving force exists in the calcite-dolomite system, though this cannot be discounted due to the evidence for Mg^{2+} migration during deformation.

CPO development in the grain size sensitive field has been observed in dolomite (Delle Piane et al., 2009a), calcite (Rutter et al., 1994a), olivine (Hansen et al., 2011; Sundberg and Cooper, 2008), orthopyroxene (Sundberg and Cooper, 2008), forsterite (Miyazaki et al., 2013), and ice (Goldsby and Kohlstedt, 2001). A CPO may occur in response to dislocation creep accommodating relative grain boundary displacements (Ashby and Verrall, 1973; Langdon, 2006). However, Miyazaki et al. (2013) show that grain boundary orientation is often crystallographically controlled with grain boundary sliding (GBS) frequently occurring on

specific planes. CPO development can, therefore, be a by-product of grain rotation by GBS (Miyazaki et al., 2013). Critically, interface-controlled diffusion creep can lead to CPO development despite little dislocation mobility; grain boundary sliding may be favoured in systems where grain boundary anisotropy is significant thus precluding dislocation creep as the dominant deformation mechanism (Sundberg and Cooper, 2008). Our J-indices are similar to those calculated for Solnhofen limestone (Barnhoorn et al., 2005a) and fine-grained calcite-dolomite composites (Delle Piane et al., 2009a) deformed to high shear strains; they are significantly lower than those reported in synthetic, fine-grained calcite aggregates deformed to high shear strains (Barnhoorn et al., 2005a). This likely results from the presence of a second phase in our samples that curtails grain growth in the material, keeping the grain size small (Barnhoorn et al., 2005a; Herwegh and Kunze, 2002; Olgaard, 1990) and hindering pervasive dislocation mobility. Indeed, even nano-scale second phases are sufficient to pin grain boundaries (Herwegh and Kunze, 2002); the fine-grained dolomite and minor accessory phases in our samples are likely sufficient to pin grain boundaries, hampering grain growth and keeping grain boundary sliding a dominant mechanism. The strength of the CPO for the calcite aggregates and the lack of subgrains are consistent with grain boundary sliding assisted by limited dislocation glide/creep (Rutter et al., 1994b; Schmid et al., 1987). Increased Mg^{2+} mobility from dolomite to calcite (see Figure 14 and Supplementary Material) suggests that diffusion processes are also active during deformation of our samples.

The microstructure and texture of calcite aggregates in all run products in this study supports grain boundary sliding accommodated by diffusion creep and possible dislocation glide/creep (Ashby and Verrall, 1973; Casey et al., 1997; Langdon, 2006; Mukherjee, 1975; Schmid et al., 1977). Grain boundary diffusion results in the subtle elongation of calcite grains and the solid-state diffusion processes that accommodate Mg^{2+} movement from dolomite into calcite (Delle Piane et al., 2009a; Langdon, 2006). This is consistent with the more pronounced grain elongation and Mg^{2+} movement observed in Dm75. Similar microstructures and textures have been published on both 100%, fine-grained calcite (Casey et al., 1997; Schmid et al., 1977) and fine-grained dolomite-calcite composites (Delle Piane et al., 2009a) and the same deformation mechanisms have been proposed.

The most dolomite-rich experiment (P1538; Dm75) shows a mixed response to deformation: fracture in dolomite and plastic flow of calcite. Mechanically, the Dm75 composite is the strongest and the most complex: the material sustained a stress drop followed by the attainment of stable flow after a shear strain of ~1, followed by an episode of strain hardening

and strain softening (Figure 7A). The rheological behaviour of Dm75 is better described by power law creep of calcite with Mohr Coulomb behavior in dolomite. The stress drop in Dm75 may have been a result of fracture of dolomite and reconfiguration of the material to attain an interconnected network of calcite, thereby attaining stable flow.

7.3 Deformation of Two-Phase Aggregates

In our study, calcite is the weak phase. The addition of a second phase to a calcite matrix can both strengthen (Austin et al., 2014; Barnhoorn et al., 2005b; Delle Piane et al., 2009a; Delle Piane et al., 2009b; Rybacki et al., 2003) and weaken (Austin et al., 2014; Delle Piane et al., 2009a) the composite aggregate. In fine-grained calcite aggregates that accommodate shear strain primarily by grain boundary sliding, the addition of fine-grained dolomite strengthens the aggregates at 700°C, but significantly weakens them at 800°C (Delle Piane et al., 2009a). This strength inversion results from a loss of competence in fine-grained dolomite at high temperatures and both dolomite and calcite deform by grain sensitive flow (Delle Piane et al., 2009a). Our samples show significant strengthening with increasing dolomite content. This is, in large part, due to the significant size of the dolomite grains, which act as rigid bodies and restrict calcite flow in our samples.

Initially homogeneous, fine-grained, two-phase aggregates (e.g. anhydrite-calcite, forsterite-pyroxene, and forsterite-diopside) develop compositional layering at high strain (Barnhoorn et al., 2005a; Hiraga et al., 2013; Miyazaki et al., 2013). In fine-grained forsterite-pyroxene aggregates, grain boundary sliding was shown to encourage ‘demixing’ of the mineral phases through grain switching events, giving rise to compositional layering (Hiraga et al., 2013). In our samples, the low-dolomite content (Dm 25 and Dm35) aggregates show compositional layering at high strains. We attribute this layering to the deformation of the spherical calcite aggregates present in the starting material and the segregation of coarse-grained dolomite. We do not observe convincing ‘demixing’ of phases within our aggregates, probably due to the large grain size of dolomite, which precludes the dolomite from participating in grain boundary sliding. The 75% dolomite content sample has a crude compositional foliation (because of dolomite grain size differentiation) defined by predominantly calcite and finer-grained dolomite grains, alternating with coarse-grained dolomite. Because of their bimodal grain size distribution (fine-grained calcite and coarse-grained dolomite) the behaviour of our samples is not consistent with the ‘demixing’ of phases via grain switching events but instead by mechanical sorting based on grain size.

7.4 Calcite Aggregates: Analogues for Veins in Nature?

EBSD analysis of the compositionally homogeneous calcite bands present in P1527 and P1524 (Figures 8A, 8B, and 12) show stronger CPOs in these regions than in the surrounding calcite-dolomite matrix. This suggests that these layers record more applied shear strain (Rutter et al., 1994b). Additionally, the presence of deflected foliations suggests strain partitioning and localization (refer to Figure 8B): areas rich in dolomite accommodated less displacement (i.e. are less sheared) than monomineralic calcite layers. Strain partitioning may occur because compositionally homogeneous regions are more easily deformed as grain boundary pinning is not encouraged (Olgaard, 1990). This results in the maintenance of the initial compositional zoning of the samples.

These calcite regions provide an interesting analog for calcite veins in nature that are observed to absorb more strain than the surrounding host rock (Kennedy and White, 2001). Low chemical potential gradients between single phase grains inhibit diffusion processes, leading to the activation of dislocation glide and, ultimately, back-stressing from the pileup of dislocations at grain boundaries, resulting in a population of strain free grains with similar CPO (Kennedy and White, 2001; Molli et al., 2011). This effect is more pronounced in pure calcite regions of Dm25 and Dm35 because the chemical potential gradients between grains are such that diffusion processes are curtailed (Kennedy and White, 2001).

8. Conclusions

The styles and mechanisms of deformation associated with many variably dolomitized limestone shear systems are strongly controlled by strain partitioning between dolomite and calcite. The contrasting deformation behaviour of dolomite and calcite aggregates in our experiments is fundamentally related to grain size. Fine-grained calcite (and possibly dolomite) deform by grain boundary sliding assisted by diffusion creep and possible limited dislocation glide. In low dolomite composites, dolomite grains act to increase the strength of shear zones relative to 100% calcite, presumably because the fine-grained calcite must flow around rigid dolomite grains.

In high dolomite content samples, two deformation mechanisms likely occur concomitantly (either in parallel or in series) during shear: brittle failure of dolomite and superplastic flow of calcite. We infer that strain hardening occurs until dolomite grains fracture permitting interconnected, fine-grained calcite to form crude layers such that grain boundary sliding of fine-grained calcite accommodates displacement. This results in extreme localization

of shear strain into thin, discontinuous calcite layers. These calcite layers are periodically obstructed by clusters of coarse-grained dolomite leading to further locking of the system. With increased dolomite content, a stress exponent greater than 3 indicates that 75% dolomite can still be described by power-law models, however, based on the microstructure, brittle deformation (Mohr –Coulomb) should be considered to act intermittently during shear strain.

These observations are critical to the interpretation of fault systems where dolomite may periodically inhibit flow in calcite networks, thereby locking the fault system and resulting in the build up of shear stresses. We speculate that the embrittlement of dolomite within these zones may be necessary in the re-establishment of grain boundary sliding networks in calcite leading to a continued ductile response of such systems.

Acknowledgements:

Our sincerest thanks are extended to J.K. Russell for his advice and support during the experimental program and writing process. Special thanks to Rolf Bruijn and Richard Bakker for their technical assistance and support during the deformation experiments at ETH-Zürich. Chadwick Sinclair, Jacob Kabel, and Jacques Precigout are sincerely thanked for their assistance and advice regarding EBSD analysis. Edith Czech and Jenny Lai are thanked for technical support during SEM and microprobe work. This manuscript benefited greatly from the editorial guardianship of Ian Alsop and enriching reviews from Auke Barnhoorn and an anonymous reviewer. TEM analysis was carried out at the Microscopy and Microanalysis Facility at the University of New Brunswick. Funding for Alexandra Kushnir was provided by the Alexander Graham Bell Canada Scholarship from the National Sciences and Engineering Research Council of Canada and Campus France. J.C. White and L.A. Kennedy were independently funded by National Sciences and Engineering Research Council of Canada Discovery Grants.

Figure Captions

Figure 1. Grain size distributions (vol.%) of starting material powders. A. Grain size distributions of pure calcite and pure dolomite powders. Modal grain sizes of the calcite and dolomite powders are 9 μm and 120 μm, respectively. B. Grain size distributions of calcite-dolomite powder mixtures used for fabricating the synthetic composites.

Figure 2. Scanning electron microscopy (SEM) and electron backscatter diffraction (EBSD) analysis of Dm25 and Dm75 starting materials after synthesis. The a and b axes refer to the axes on the stereographic projections. The cold pressing direction is parallel to the canister length, into the page. A. Dm25; Equiaxed calcite grains, closely packed with straight grain boundaries forming triple junctions. There is significant residual intergranular porosity at calcite grain boundaries. B. Dm25; Lower hemisphere contoured stereoplots for the c slip system for calcite (left) and dolomite (right). N is the number of grains used to produce the pole figures, J is the J-texture index, and pfJ is the pole figure J-texture index, reflecting texture strength of the c-slip system. C. Dm75; Equiaxed calcite grains, closely packed with straight grain boundaries forming triple junctions. Residual porosity is concentrated at dolomite boundaries. D. Dm75. Lower hemisphere contoured stereoplots for the c slip system for calcite (left) and dolomite (right). N is the number of grains used to produce the pole figures, J is the J-texture index, and pfJ is the pole figure J-texture index, reflecting texture strength of the c-slip system. Note the large variation in dolomite grain size that is also common in naturally formed dolomitic limestones.

Figure 3. Backscatter electron images of a pure calcite spherical aggregate in Dm35 starting material. A. The diameter of the imaged aggregate is ~200 μm. B. High aspect ratio dolomite grains are oriented such that their long axes are tangential to the circumference of the aggregate. The dashed white line identifies the boundary between pure calcite and calcite-dolomite. Porosity within the aggregate is homogeneously distributed and occurs along calcite grain boundaries, specifically at triple junctions.

Figure 4. Grain size distributions (area fraction) of calcite (A) and dolomite (B) from coherent, hot isostatically pressed starting material and high strain experiments (Dm25, P1527; Dm75, P1538) measured using SEM and EBSD techniques.

Figure 5. A. Schematic of the Paterson deformation apparatus with torsion actuator (modified from Paterson and Olgaard, (2000)). B. Schematic diagram of the two principal thin section cuts used in this study (Paterson and Olgaard, (2000)). The longitudinal axial cut captures intermediate strains along the centre axis of the segment. The longitudinal tangential segment captures the maximum strain plane of the sample. d and l are the diameter and length of the perfect cylindrical sample, respectively.

Figure 6. Log-log plot of shear strain rate vs. torque from the strain rate stepping experiments for A. Dm25 and Dm35 and, B. Dm75; the slope of the lines of best fit are the *n*-values (stress exponent, Eq. (4)) for the given compositions. Experimental conditions: T=750˚C; P_{eff} = 262 MPa.

Figure 7. Mechanical data for A. high-strain-rate experiments and B. low-strain-rate experiments. See Table 2 for experimental conditions. High-strain-rate experiments: P1522 (Dm25), P1524 (Dm35), P1525 (Dm75), P1527 (Dm25), P1528 (Dm51), P1537 (Dm51), and P1538 (Dm75). The heating history of experiment P1537 (Dm51) is not known for shear strains above 2, therefore, this data is omitted. Low strain experiments: P1523 (Dm51), P1533 (Dm75), and P1543 (Dm35). C. Shear stress as a function of dolomite content. Shear stress increases with dolomite content. Triangles denote yield stress; squares denote the shear stress at a shear strain equal to 1.5; circles denote peak shear stress. Shear stresses for 0%, 9%, 40%, and 100% dolomite contents are taken from Barnhoorn et al. (2005a), Delle Piane et al. (2009a), Davis et al. (2008), and Holyoke et al. (2013). Equivalent shear stresses for the reported differential stresses in Davis et al. (2008) and Holyoke et al. (2013) were calculated using Paterson and Olgaard (2000).

Figure 8. SEM images. Dolomite is the larger, dark grey phase. Calcite makes up the light grey matrix. Pyrite is white. High strain, deformed material: Dm25; P1527; γ~5; 750˚C; 3x10^{-4} s^{-1}. Longitudinal tangential plane (refer to Figure 5B). The shear zone boundary is horizontal in all images. A. Foliation is defined by elongate calcite aggregates (dashed ellipse). Shear strain is calculated by $\gamma = \cot\alpha' - \cot\alpha$. B. The foliation in the bulk calcite-dolomite matrix is deflected and converges with the higher strained pure-calcite band (oriented sub-parallel to the shear zone boundary). Dashed white lines delineate the bulk foliation within the sample. Dashed black line delineates the boundaries of the pure-calcite band. C. C-s mylonite texture. Foliation is defined

by surfaces of apparent localized strain (black rectangle), elongate pyrite grains, and rotated, high aspect ratio dolomite grains (black arrows). Dolomite grains are organized along both s- and c-foliations and are not obviously rounded. D. Localised c-surfaces appear as thin, dark, discontinuous layers defined by ultrafine-grained material. A selection of c-surfaces are highlighted by arrows. E. Closely packed, equiaxed to tabular calcite-grains. Grain boundaries form triple junctions and are generally straight. Note significant isolated porosity. F. Considerable isolated porosity located within 'pressure shadow'-like regions of dolomite grains.

Figure 9. SEM images. Dolomite is the larger, dark grey phase. Calcite makes up the light grey matrix. Pyrite is white. High strain deformed material: Dm75. P1538; γ~5; 750˚C; $3x10^{-4}$ s^{-1}. Longitudinal tangential plane (refer to Figure 5B); the shear zone boundary (SZB) is horizontal in all images. A. Patchy foliation development in Dm75 where tabular dolomite is rotated to define a shape fabric (centre of the image). The pyrite grain in the top left hand corner (white) has been boudinaged and deformed around the more rigid dolomite grain. The white ellipse highlights a dolomite grain that has fragmented by shear fracture during sinistral shear. B. Closely packed, equiaxed to elongate calcite grains. Rounded, tabular dolomite grains are rotated into foliation. C. Evidence of ductile deformation. The dashed black line defines the local foliation developed within the calcite matrix. The foliation is deflected around large dolomite grains. A highly sheared pyrite grain is identified by the white arrow. D. Antithetic shear fracture of a large dolomite grain.

Figure 10. EBSD analysis of high strain experiments, Dm25 (P1527) and Dm75 (P1538). The shear zone boundary (SZB) is horizontal in all images and pole figures. N is the number of grains used to produce the pole figures, J is the J-texture index, and pfJ is the pole figure J-texture index, reflecting texture strength of the individual slip systems. A. Dm25; low magnification BSE image. B. Dm25. Calcite: EBSD map (top); lower hemisphere contoured stereoplots (bottom) for the c and a slip systems. C. Dm25. Dolomite: EBSD map (top); lower hemisphere contoured stereoplots (bottom) for the c and a slip systems. Blackened portions of the EBSD maps are components of different phases, not indexed. See text for details. D. Dm75; low magnification BSE image. E. Dm75. Calcite: EBSD map (top); lower hemisphere contoured stereoplots (bottom) for the c and a slip systems. F. Dm75. Dolomite: EBSD map (top); lower hemisphere contoured stereoplots (bottom) for the c and a slip systems. Blackened portions of the EBSD maps are components of different phases, not indexed. See text for details.

Figure 11. Transmission electron microscopy (TEM BF). A. Glide dislocations within calcite grain. B. Equant grain texture in deformed calcite consistent with grain boundary sliding (superplasticity). Despite the absence of grain shape change (elongation), there are high dislocation densities within individual grains, suggesting creep accommodated grain boundary sliding.

Figure 12. Crystallographic preferred orientation development near calcite aggregates. The shear zone boundary (SZB) is horizontal in all BSE images and EBSD maps. N is the number of grains used to produce the pole figures, J is the J-texture index, and pfJ is the pole figure J-texture index, reflecting texture strength of the individual slip systems. All pole figures are lower hemisphere projections. A. BSE image of Dm25 sample deformed to γ~5.5 (see Table 2; P1527). A calcite sphere that has been sheared into an ellipsoid is delineated by the red lines. B. EBSD map and stereonet projection of the c and a slip systems in calcite across the deformed calcite band. C. EBSD map and steronet projection of calcite in a region removed from the calcite band. D. EBSD map and stereonet projections of a region adjacent to the calcite band, but including dolomite grains. E. EBSD map and stereonet projection of a region within the calcite band.

Figure 13. Evolution of crystallographic preferred orientation (CPO) of the c-axis slip system in calcite with strain. Stress-strain curves represent the stress-strain conditions at the sample edge. Stereonets are lower hemisphere projections; shear zone boundary (SZB) is horizontal. For a given composition, each stereonet is produced by analysing a different longitudinal axial section from the same deformed core (see Figure 5B), thus representing the state of the material at different shear strains. N is the number of grains used to produce the pole figures, J is the J-texture index, and pfJ is the pole figure J-texture index, reflecting texture strength of the c-axis slip system. Red dots indicate the approximate points on the stress-strain curve that correspond to the longitudinal axial cuts made. CPO becomes more defined with increasing shear strain (i.e. the c-axis girdle becomes more narrow with increasing strain and the J- and pfJ-indices generally increase, with the exception of C). A. Dm25 (P1527). B. Dm35 (P1524). C. Dm75 (P1538).

Figure 14 Energy-dispersive X-ray spectroscopy (EDS) maps of magnesium concentration for experiment P1527. Experimental conditions: P_{eff}=262 MPa, T=750˚C, and strain rate $3x10^{-4}$ s^{-1}. The shear zone boundary (SZB) is horizontal in all images. A. EDS map of a longitudinal axial

783 section of the sample corresponding to γ~0 (see Figure 5B). B. EDS map of a longitudinal axial
784 section of the sample corresponding to γ~2.25. C. EDS map of the longitudinal tangential section
785 of the sample, corresponding to γ~5.5. White grains are dolomite. The calcite matrix contains
786 very little magnesium and, therefore, is black. For γ~0, there is no magnesium observed within
787 the matrix. With increasing strain, Mg^{2+} concentrations increase in the matrix; note the increase
788 in white streaking between dolomite grains in B and C. This only occurs in regions of the sample
789 with locally significant fine-grained dolomite content. With increasing shear strain, Mg^{2+}
790 becomes more concentrated along the developing foliation of the sample.
791
792 Figure 15 A. Comparison of the study data with the reported deformation mechanism map of
793 Solnhofen limestone (taken from Schmid et al., 1977). Log-log plot of the differential stress vs.
794 strain rate for compression deformation experiments on Solnhofen limestone. Regime 1:
795 Exponential relationship between strain rate and stress; Regime 2: Power-law creep; Regime 3:
796 Superplasticity. Regimes 1 and 2 are characterized in the microstructure by dislocation glide
797 and/or dislocation creep. Regime 3 is characterized in the microstructure by grain boundary
798 sliding. Triangles indicate data from this study. With increasing differential stress, these triangles
799 represent the peak strengths of Dm25, Dm35, Dm51, and Dm75. The square and circle indicate
800 the peak stress for Solnhofen limestone deformed by torsion to high strains at 700˚C and 800˚C,
801 respectively (Schmid et al., 1987). B. Comparison of study data with reported deformation
802 behaviour of Madoc dolomite (Davis et al., 2008; Holyoke et al., 2013). The deformation
803 mechanism map is taken from Holyoke et al. (2013) and is contoured for dolomite grain size.
804 The contours denote the transition between dislocation creep and diffusion creep. Experiment
805 P1538 (Dm75, taken to high strain) is plotted as a triangle and lies in the diffusion creep field for
806 dolomite grain sizes <10 μm and the dislocation creep field for dolomite grain sizes >100 μm.
807 The square and circle represent the differential stress of Madoc dolomite (grain size = 240 μm) at
808 700˚C (Davis et al., 2008) and 900˚C (Holyoke et al., 2013), respectively.
809

References

Ashby, M.F., Verrall, R.A., 1973. Diffusion-accommodated flow and superplasticity. Acta Metall. 21, 149-163.

Austin, N.J., 2003. An experimental investigation of textural controls on the brittle deformation of dolomite, Eartha nd Ocean Sciences. University of British Columbia, Vancouver.

Austin, N.J., Evans, B., Rybacki, E., Dresen, G., 2014. Strength evolution and the development of crystallograpgic preferred orientation during deformation of two-phase marbles. Tectonophysics 631, 14-28.

Austin, N.J., Kennedy, L.A., 2005. Textural controls on the brittle deformation of dolomite: variations in peak strength. Geological Society Special Publication, 37-49.

Austin, N.J., Kennedy, L.A., Logan, J.M., Rodway, R., 2005. Textural controls on the brittle deformation of dolomite: The transition from brittle faulting to cataclastic flow. Geological Society Special Publication, 51-66.

Bachmann F., H., R., Schaeben, H., 2010. Texture Analysis with MTEX - Free and Open Source Software Toolbox. Solid State Phenomena 160, 63-68.

Barnhoorn, A., 2003. Rheological and microstructural evolution of carbonate rocks during large strain torsion experiments. Swiss Federal Institute of Technology Zurich, ETH Zurich.

Barnhoorn, A., Bystricky, M., Burlini, L., Kunze, K., 2005a. Post-deformational annealing of calcite rocks. Tectonophysics 403, 176-191.

Barnhoorn, A., Bystricky, M., Kunze, K., Burlini, L., Burg, J.P., 2005b. Strain localisation in bimineralic rocks: Experimental deformation of synthetic calcite-anhydrite aggregates. Earth and Planetary Science Letters 240, 748-763.

Bestmann, M., Kunze, K., Matthews, A., 2000. Evolution of a calcite marble shear zone complex on Thassos Island, Greece: microstructural and textural fabris and their kinematic significance. Journal of Structural Geology 22, 1789-1807.

Casey, M., Kunze, K., Olgaard, D.L., 1997. Texture of Solnhofen limestone deformed to high strains in torsion. Journal of Structural Geology 20, 255-267.

Coble, R.L., 1963. A model for boundary diffusion controlled creep in polycrystalline materials. Journal of Applied Physics.

Davis, N.E., Kronenberg, A.K., Newman, J., 2008. Plasticity and diffusion creep of dolomite. Tectonophysics, 127-146.

Delle Piane, C., Burlini, L., Kunze, K., 2009a. The influence of dolomite on the plastic flow of calcite: Rheological, microstructural and chemical evolution during large strain torsion experiments. Tectonophysics, 145-166.

Delle Piane, C., Burlini, L., Kunze, K., Brack, P., Burg, J.P., 2008. Rheology of dolomite: Large strain torsion experiments and natural examples. Journal of Structural Geology 30, 767-776.

Delle Piane, C., Wilson, C.J.L., Burlini, L., 2009b. Dialatant plasticity in high-strain experiments on calcite-muscovite aggregates. Journal of Structural Geology, 1084-1099.

Erikson, S.G., 1994. Deformation of shale and dolomite in the Lewis Thrust-fault zone, Northwest Montana, USA. Cannadian Journal Earth Sciences 31, 1440-1448.

Gifkins, R.C., 1976. Grain-boundary sliding and its accommodation during creep and superplasticity. Metallurgical Transactions A-Physical Metallurgy and Material Science 7, 1225-1232.

Goldsby, D.L., Kohlstedt, D.L., 2001. Superplastic deformation of ice: Experimental observations. Journal of Geophysical Research, 11017-11030.

Goldsmith, J.R., 1959. Some aspects of the geochemistry of carbonates.

Griggs, D.T., Turner, F.J., Borg, I., Sosoka, J., 1951. Deformation of Yule marble, part iV. Effects at 150C. GSA Bulletin 62, 1385-1486.

858 Griggs, D.T., Turner, F.J., Borg, I., Sosoka, J., 1953. Deformation of Yule marble, part V.
859 Effects at 300C. GSA Bulletin 64.
860 Handin, J., Fairburn, H.W., 1955. Experimental deformation of Hasmark dolomite. GSA Bulletin
861 66, 1257-1274.
862 Hansen, L.N., Zimmerman, M.E., Kohlstedt, D.L., 2011. Grain boundary sliding in San Carlos
863 olivine: Flow law parameters and crystallographic-preferred orientation. Journal of Geophysical
864 Research 116.
865 Herwegh, M., De Bresser, J.H.P., ter Heege, J.H., 2005. Combining natural microstructures with
866 composite flow laws: an improved approach for the extrpolation of lab data to nature. Journal of
867 Structural Geology, 503-521.
868 Herwegh, M., Kunze, K., 2002. The influence of nano-scale second-phase particles on
869 deformation of fine grained calcite mylonites. Journal of Structural Geology 24, 1463-1478.
870 Herwegh, M., Xiao, X., Evans, B., 2003. The effect of dissolved magnesium on diffusion creep
871 in calcite. Earth and Planetary Science Letters 212, 457-470.
872 Higgs, D.V., Handin, J., 1959. Experimental deformation of dolomite single crystals. Bulletin of
873 the Geological Society of America 70.
874 Hiraga, T., Miyazaki, T., Yoshida, H., Zimmerman, M.E., 2013. Comparison of microstructures
875 in superplastically deformed synthetic materials and natural mylonites: Minerla aggregation via
876 grain boundary sliding. Geology 41, 959-962.
877 Holyoke, C.W., Kronenberg, A.K., Newman, J., 2013. Dislocation creep of polycrystalline
878 dolomite. Tectonophysics 590, 72-82.
879 Kennedy, L.A., Logan, J.M., 1997. The role of veining and dissolution in the evolution of fine-
880 grained mylonites: the McConnell thrust, Alberta. Journal of Structural Geology 19, 785-797.
881 Kennedy, L.A., White, J.C., 2001. Low-temperature recrystallization in calcite: Mechnisms and
882 consequences. Geology 29, 1027-1030.
883 Langdon, T.G., 2006. Grain boundary sliding revisited: Developments in sliding over four
884 decades. Journal of Material Sciences, 597-609.
885 Miyazaki, T., Sueyoshi, K., Hiraga, T., 2013. Olivine crystals align during diffusion creep of
886 Earth's upper mantle. Nature 502, 321-326.
887 Molli, G., White, J.C., Kennedy, L.A., Taini, V., 2011. Low-temperature deformation of
888 limestone, Isola Palmaria, northern Apennine, Italy - The role of primary textures, precursory
889 veins and intracryatlline deformation in localization. Journal of Structural Geology, 225-270.
890 Mukherjee, A.K., 1975. High-temperature creep. Academic Press, New York.
891 Olgaard, D.L., 1990. The role of second phase in localizing deformation, in: Knipe, R.J., Rutter,
892 E.H. (Eds.), Deformation Mechanisms, Rheology and Tectonics. Geological Society Special
893 Publication, pp. 175-181.
894 Paterson, M.S., Olgaard, D.L., 2000. Rock deformation tests to large shear strains in torsion.
895 Journal of Structural Geology 22, 1341-1358.
896 Pera, E., Mainprice, D., Burlini, L., 2003. Anisotropic seismic properties of the upper mantle
897 beneath the Torre Alfina area (Northern Apennines, Central Italy). Tectonophysics, 11-30.
898 Pouchou, J.L., Pichoir, F., 1985. PAP $\phi(\rho Z)$ procedure for improved quantitative microanalysis.
899 Microbeam Analysis, 104-106.
900 Raudsepp, M., Pani, E., Dipple, G.M., 1999. Measureing mineral abundance in skarn. I. The
901 Rietveld method using X-ray powder diffraction data. Canadian Mineralogist 37, 1-15.
902 Rutter, E., 1974. The influence of temperature, strain rate and interstitial water in experimental
903 deformation of calcite rocks. Tectonophysics 22, 311-334.
904 Rutter, E., Casey, M., Burlini, L., 1994a. Preferred crystallographic orientation development
905 during the plastic and superplastic flow of calcite rocks. Journal of Structural Geology 16, 1431-
906 1446.

907 Rutter, E.H., Casey, M., Burlini, L., , 1994b. Preferred crystallographic orientation development
908 during the plastic and superplastic flow of calcite rocks. Journal of Structural Geology 16, 1431-
909 1446.
910 Rybacki, E., Paterson, M.S., Wirth, R., Dresen, G., 2003. Rheology of calcite-quartz aggregates
911 deformed to large strain in torsion. Journal of Geophysical Research 108, 2089.
912 Schmid, S.M., 1976. Rheological evidence for changes in the deformation mechanism of
913 Solnhofen limestone towards low stress. Tectonophysics 31, T21-T28.
914 Schmid, S.M., Boland, J.N., Paterson, M.S., 1977. Superplastic flow in Finegrained limestone.
915 Tectonophysics, 257-291.
916 Schmid, S.M., Panozzo, R., Bauer, S., 1987. Simple shear experiments on calcite rocks: rheology
917 and microfabric. Journal of Structural Geology 9, 747-778.
918 Sundberg, M., Cooper, R.F., 2008. Crysallographic preferred orientation produced by diffusional
919 creep of harzburgite: Effects of chimcal interactions among phases during plastic flow. Journal
920 of Geophysical Research 113.
921 Viola, G., Mancktelow, N.S., Miller, J.A., 2006. Cyclic frictional-viscous slip oscillations along
922 the base of an advancing nappe complex: Insights into brittle-ductile nappe emplacement
923 mechanisms from the Naukluft Nappe Complex, central Namibia. Tectonics 25.
924 Walker, A.N., Rutter, E.H., Brodie, K.H., 1990. Experimental study of grain-size sensitive flow
925 of synthetic, hot pressed calcite rocks, in: Knipe, R.J., Rutter, E.H. (Eds.), Deformation
926 Mechanisms, Rheology and Tectonics. Geologic Socitey Special Publications, pp. 259-284.
927 Weertman, J., 1957. Steady-state creep through dislocation climb. Journal of Applied Physics,
928 362-364.
929 Woodward, N.B., Wojtal, S., Paul, J.B., Zadins, Z.Z., 1988. Partitioning of deformation within
930 several external thrust zones of the Appalachian orogen. J. Geol. 96, 351-361.
931

Table 1. Properties of HIP samples: dolomite content (Dm), connected porosity (ϕ), density (ρ).

Dm (%)	ϕ (%)	ρ (kg m^{-3})
25	3.3±0.2	2.76
35	3.3±0.2	2.77
51	2.7±0.3	2.80
75	5.2±0.3	2.85

Table 2 List of deformation experiments performed and results.

Experiment	Dm (%)	T (°C)	P_C (MPa)	P_e (MPa)	$\dot{\gamma}$ (s^{-1})	γ_{max}	τ_{yield} (MPa)	τ_{peak} (MPa)	$\tau_{\gamma=1.5}$ (MPa)	n
Constant Strain Rate Experiments										
P1522	25	750	300	262	$3x10^{-4}$	4.4	33	79	33	
P1523	51	750	300	262	$1x10^{-4}$	1.9	17	77	-	
P1524	35	750	300	262	$3x10^{-4}$	5	33	79	33	
P1525	75	750	300	262	$3x10^{-4}$	0.16	36	117	-	
P1527	25	750	300	262	$3x10^{-4}$	5.5	27	82	27	
P1528	51	750	300	262	$3x10^{-4}$	0.21	28	79	-	
P1533	75	750	300	262	$1x10^{-4}$	0.17	44	92	-	
P1537	51	750	300	262	$3x10^{-4}$	1.7	35	135	35	
P1538	75	750	300	262	$3x10^{-4}$	5.5	57	167	37	
P1543	35	750	300	262	$1x10^{-4}$	0.1	12	63	-	
Strain Rate Stepping Experiment										
P1529	35	750	300	262	stepping	n.d.	-	-	-	2.0±0.43
P1711	25	750	300	262	stepping	n.d.	-	-	-	1.7±0.23

P1713	75	750	300	262	stepping	n.d.		3.6±0.12

n.d. not determined, Dm – dolomite content (%), T – temperature (°C), P_C – confining pressure (MPa), P_e – confining pressure (MPa), $\dot{\gamma}$ - shear strain rate (s^{-1}), γ_{max} – maximum shear stress, n – stress exponent, τ_{yield} – yield strength (MPa), τ_{peak} – peak strength (MPa), $\tau_{\gamma=1.5}$ - strength at a shear strain of 1.5 (MPa).

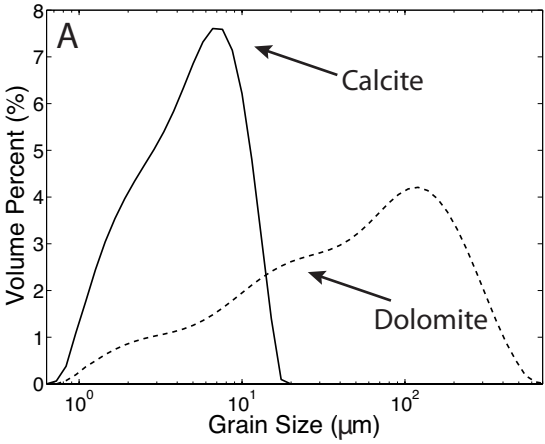

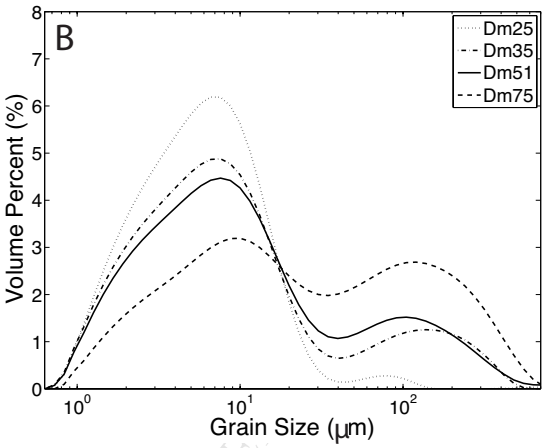

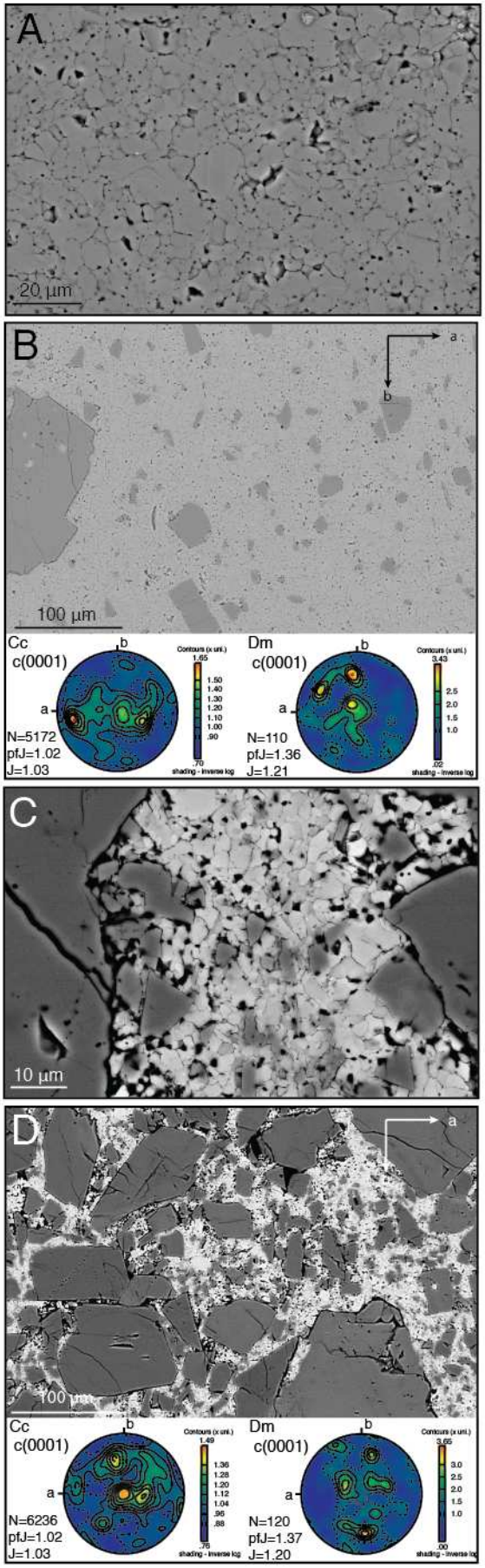
A
20 µm
B
a
b
100 µm
Cc
c(0001)
N=5172
pfJ=1.02
J=1.03
Dm
c(0001)
N=110
pfJ=1.36
J=1.21
C
10 µm
D
100 µm
Cc
c(0001)
N=6236
pfJ=1.02
J=1.03
Dm
c(0001)
N=120
pfJ=1.37
J=1.20

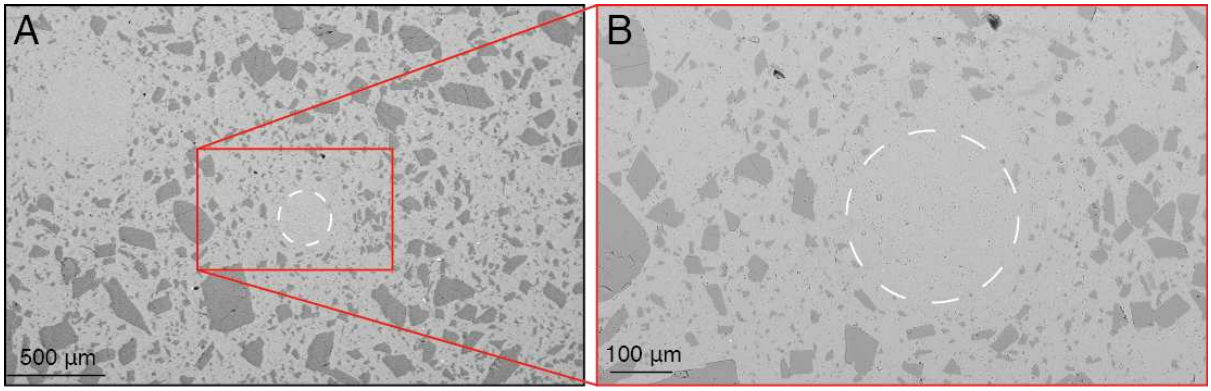

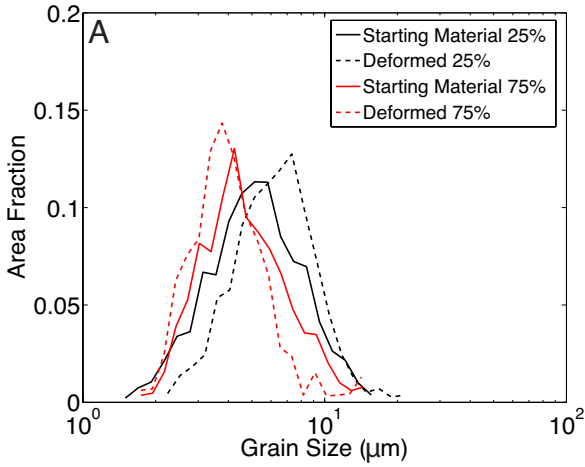
A
Starting Material 25%
Deformed 25%
Starting Material 75%
Deformed 75%
Area Fraction
0.2
0.15
0.1
0.05
0
10^0
10^1
10^2
Grain Size (μm)

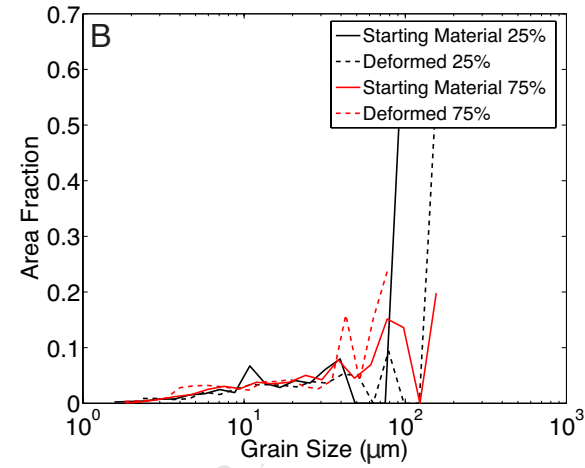
B
Starting Material 25%
Deformed 25%
Starting Material 75%
Deformed 75%
Area Fraction
0.7
0.6
0.5
0.4
0.3
0.2
0.1
0
10^0
10^1
10^2
10^3
Grain Size (μm)

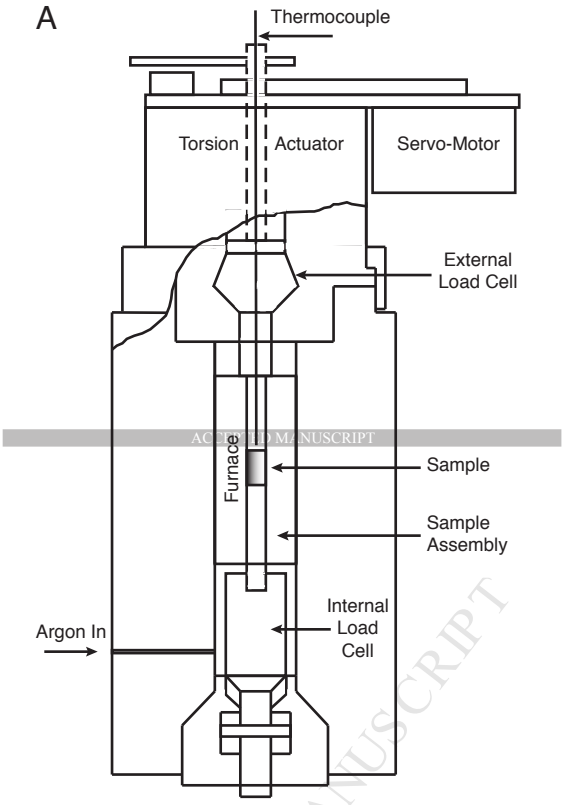

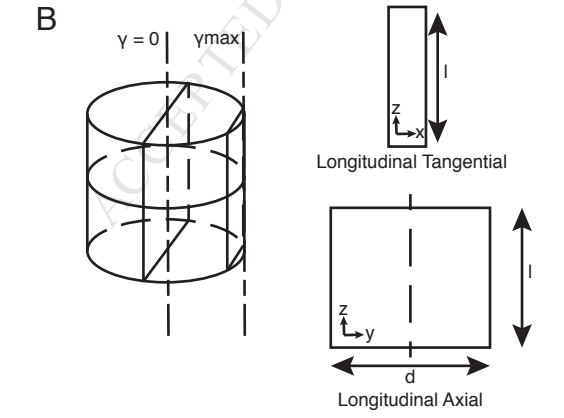

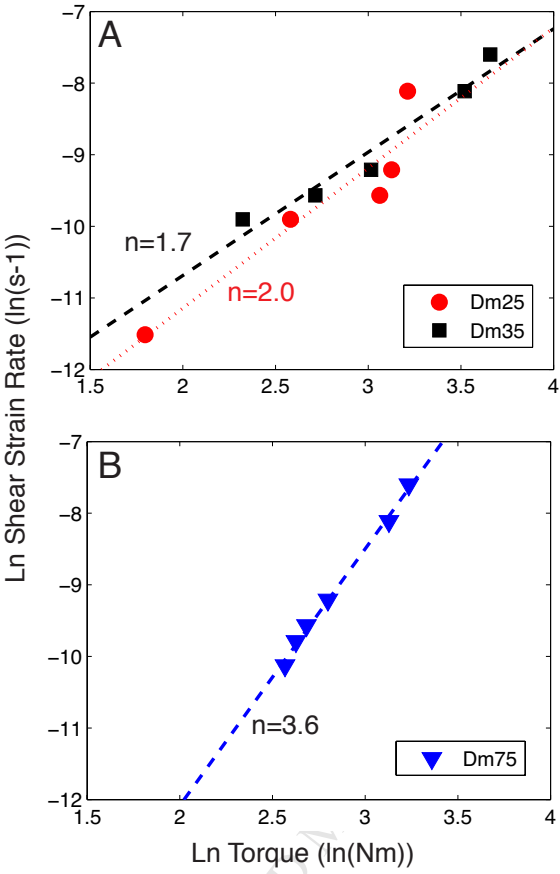
A
n=1.7
n=2.0
Dm25
Dm35
B
n=3.6
Dm75
Ln Shear Strain Rate (ln(s-1))
Ln Torque (ln(Nm))

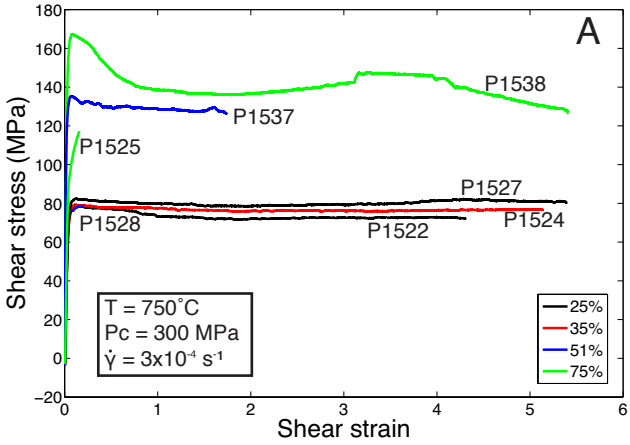
A
Shear stress (MPa)
Shear strain
P1538
P1537
P1525
P1527
P1528
P1522
P1524
T = 750˚C
Pc = 300 MPa
γ̇ = 3x10⁻⁴ s⁻¹
25%
35%
51%
75%

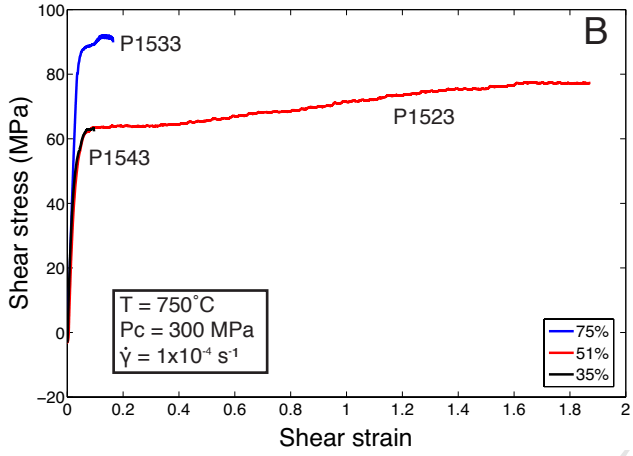
B
Shear stress (MPa)
Shear strain
P1533
P1523
P1543
T = 750˚C
Pc = 300 MPa
γ̇ = 1x10⁻⁴ s⁻¹
75%
51%
35%

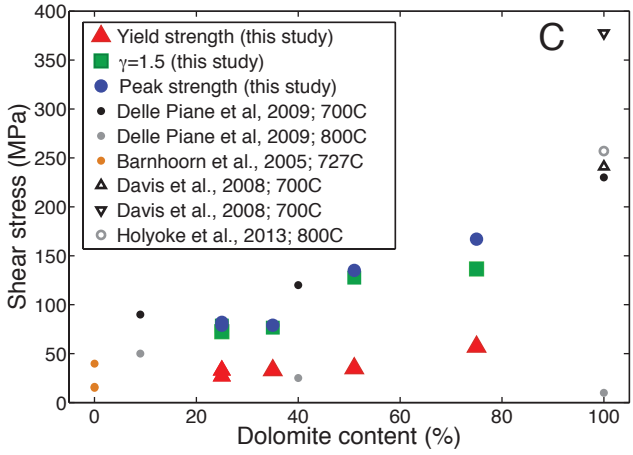
C
Shear stress (MPa)
Dolomite content (%)
Yield strength (this study)
γ=1.5 (this study)
Peak strength (this study)
Delle Piane et al, 2009; 700C
Delle Piane et al, 2009; 800C
Barnhoorn et al., 2005; 727C
Davis et al., 2008; 700C
Davis et al., 2008; 700C
Holyoke et al., 2013; 800C

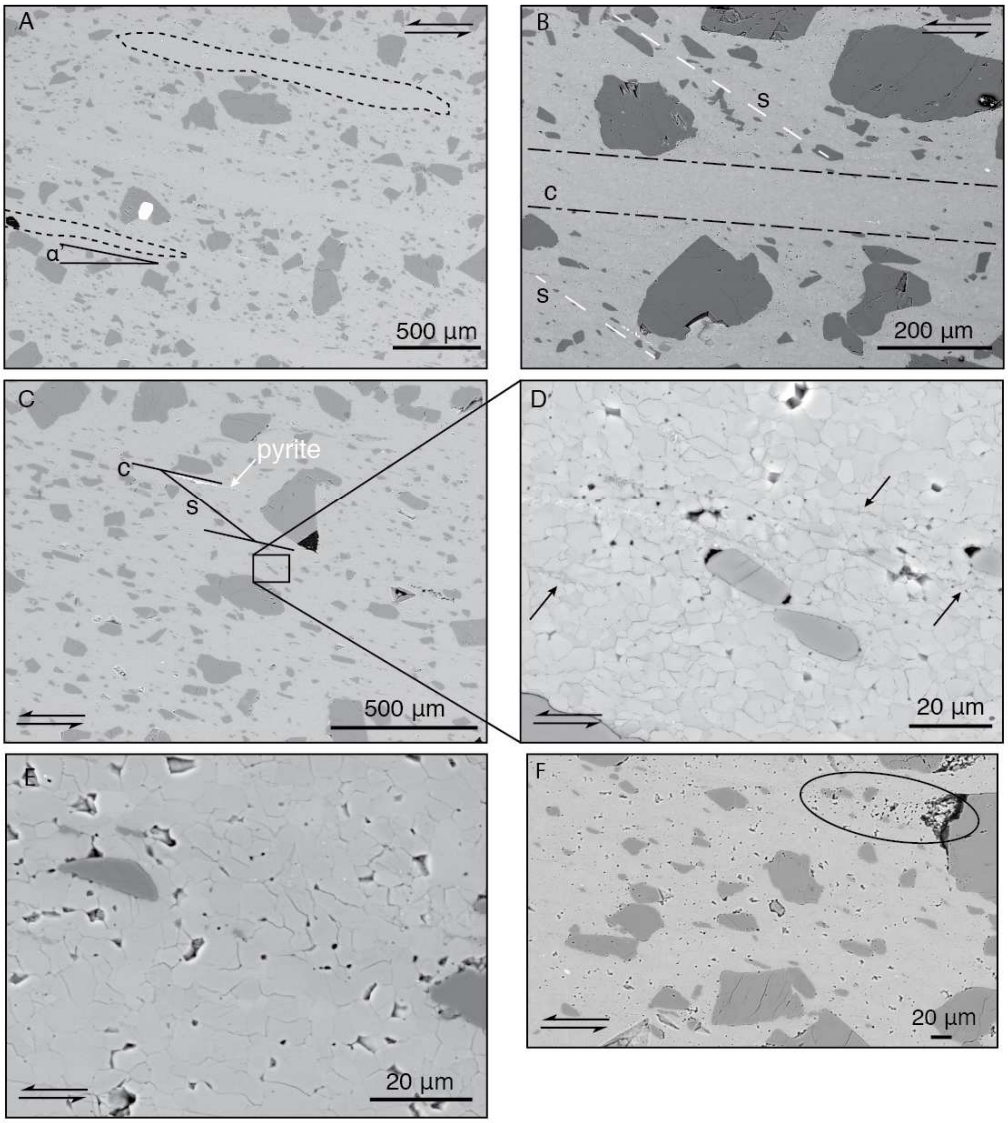

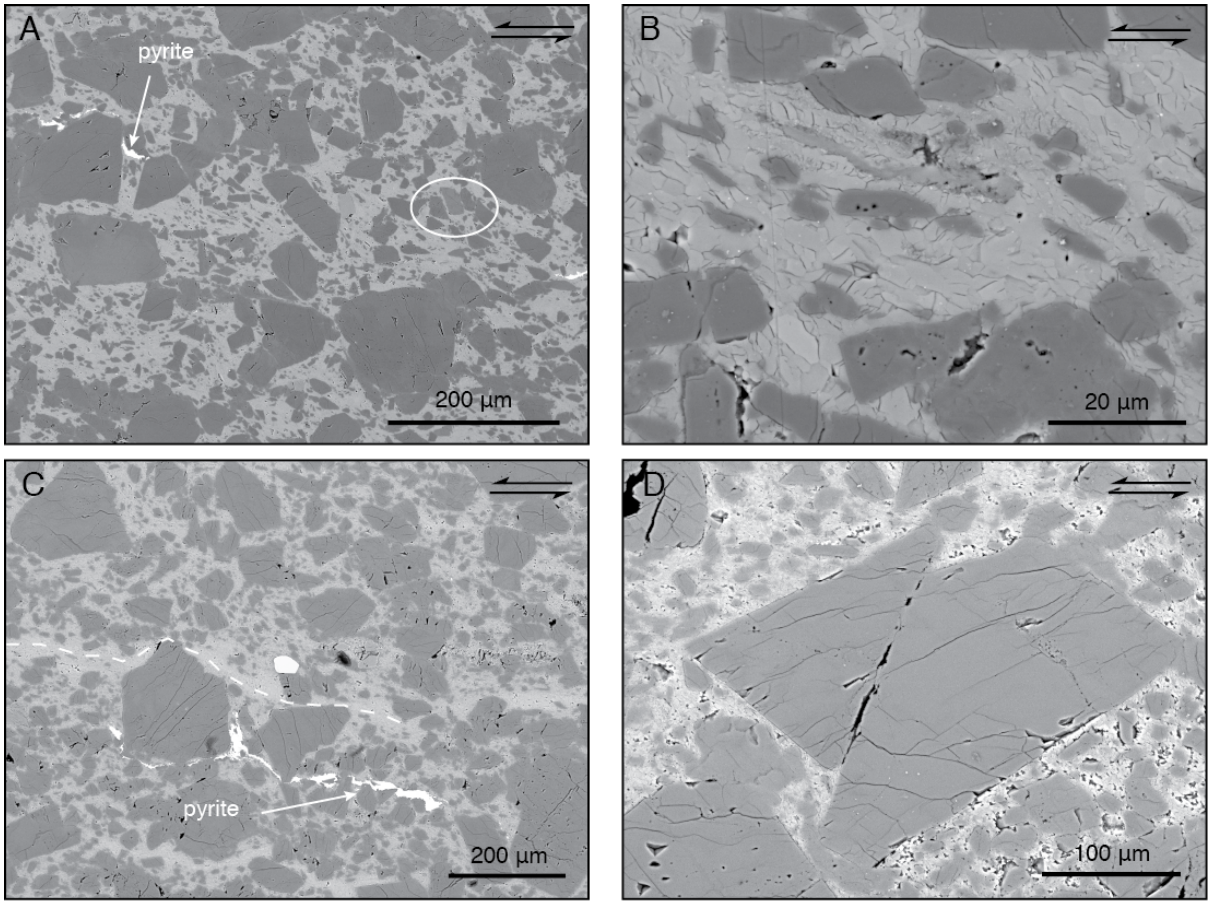

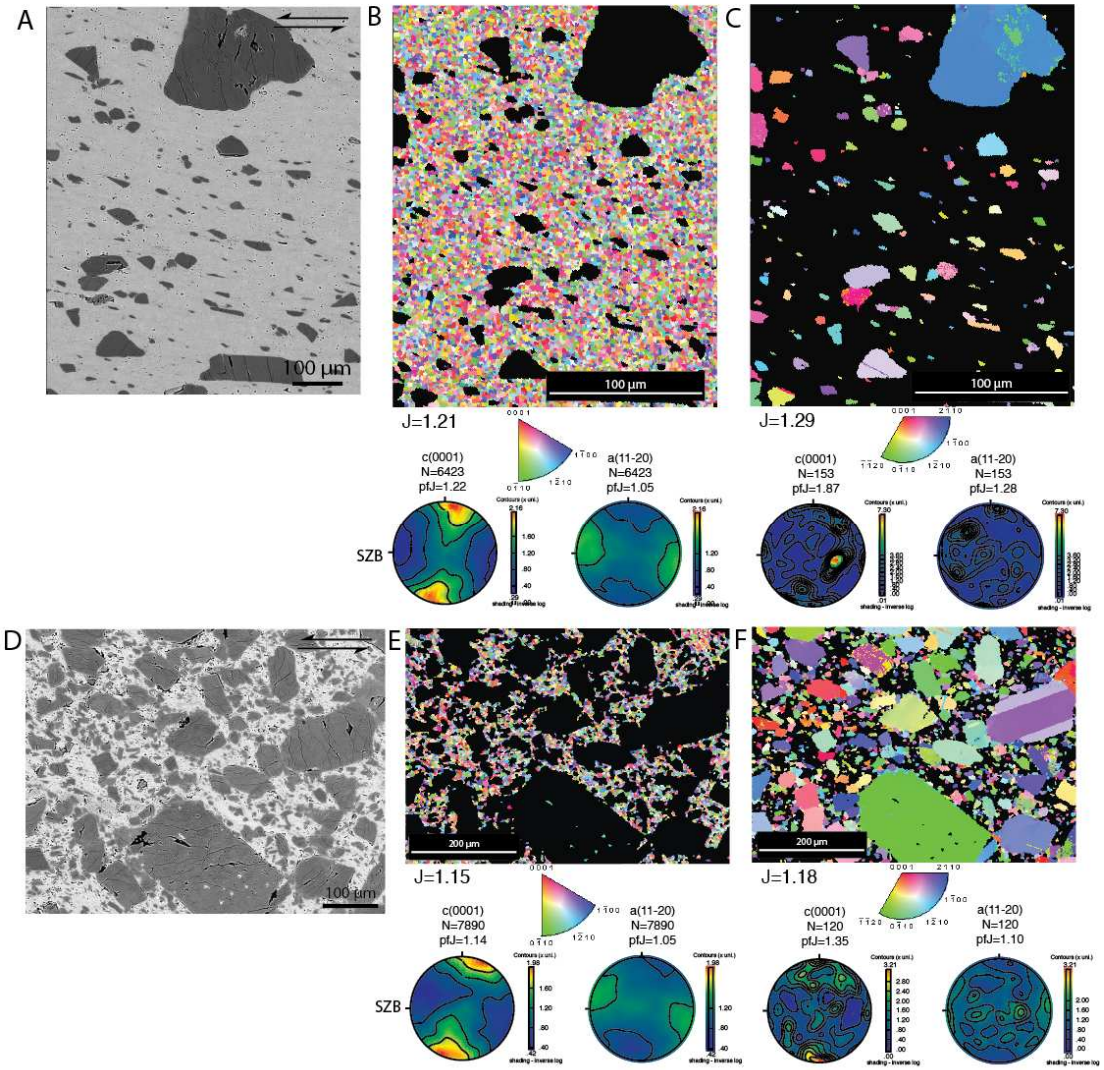
A
100 µm
B
100 µm
J=1.21
c(0001)
N=6423
pfJ=1.22
a(11-20)
N=6423
pfJ=1.05
SZB
C
100 µm
J=1.29
c(0001)
N=153
pfJ=1.87
a(11-20)
N=153
pfJ=1.28
D
100 µm
E
200 µm
J=1.15
c(0001)
N=7890
pfJ=1.14
a(11-20)
N=7890
pfJ=1.05
SZB
F
200 µm
J=1.18
c(0001)
N=120
pfJ=1.35
a(11-20)
N=120
pfJ=1.10

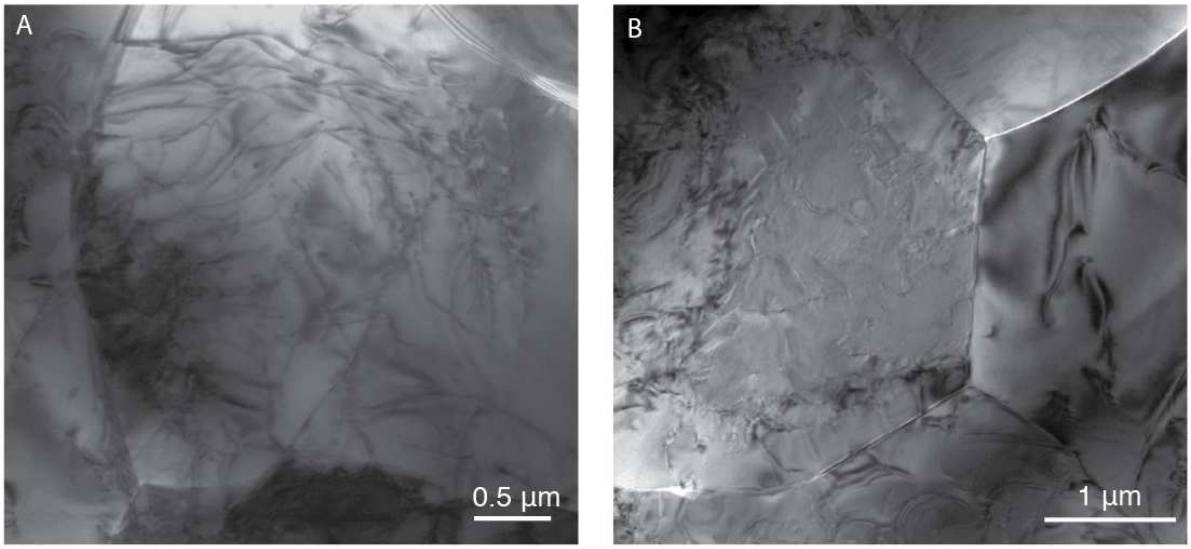

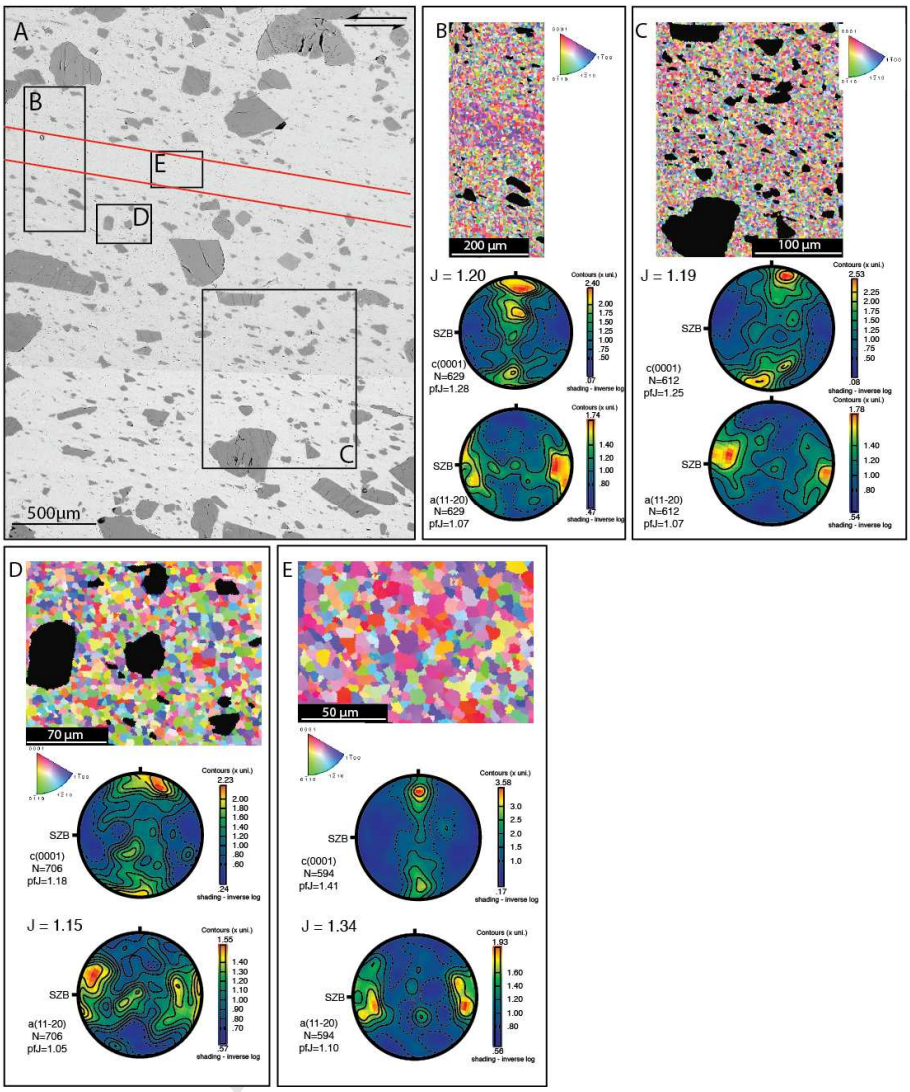

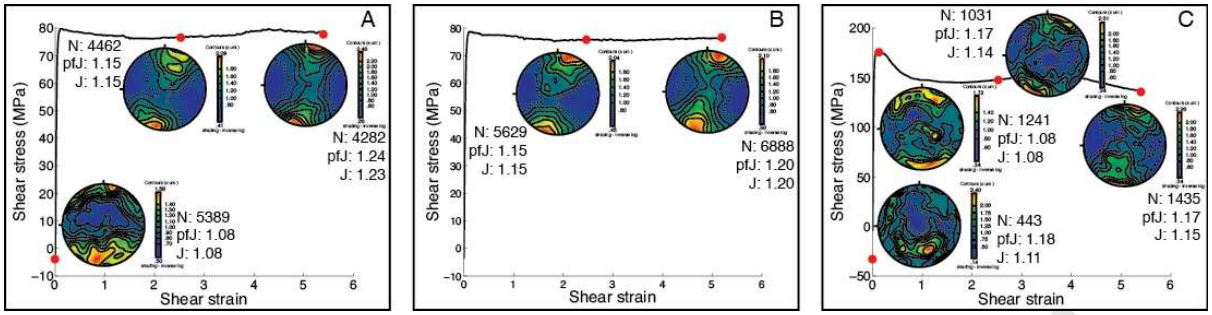

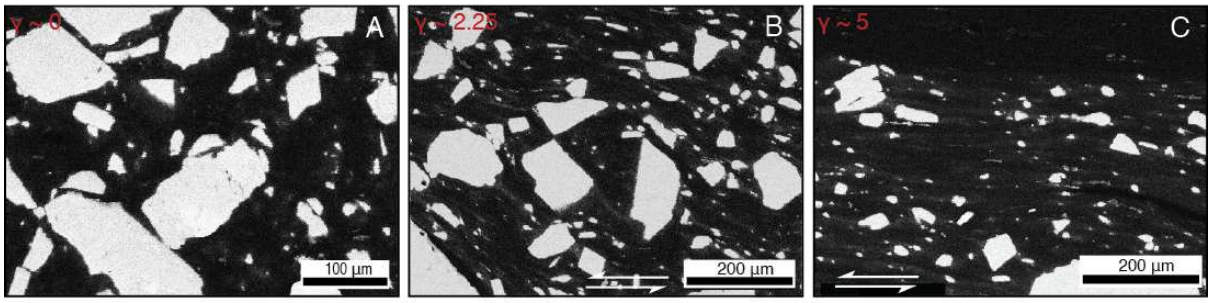

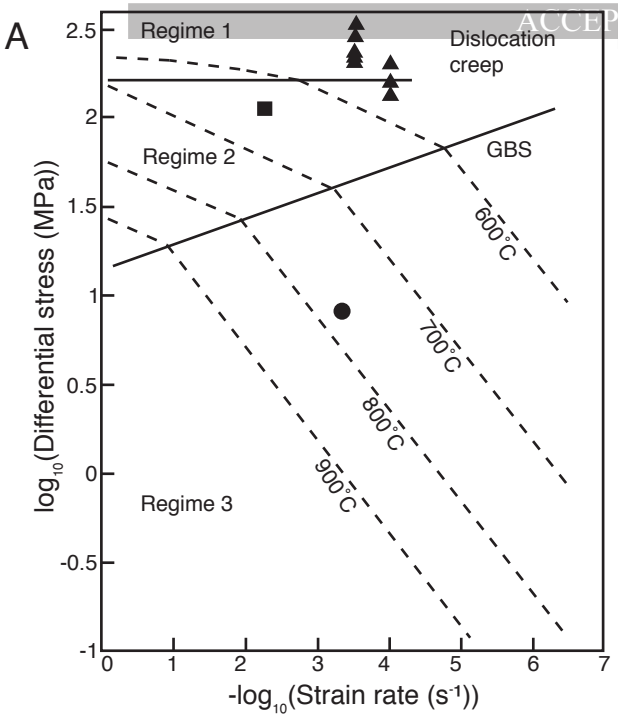

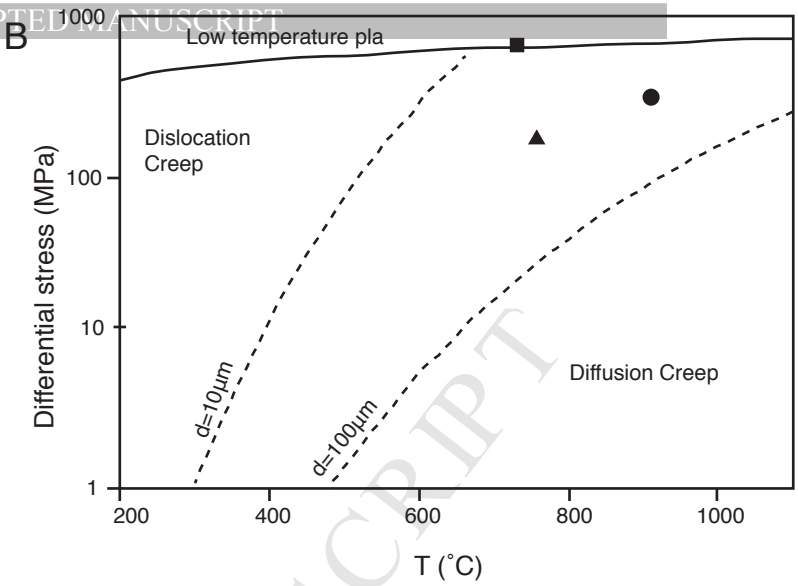

- The strength of calcite-dolomite composites increases with dolomite content.
- Calcite accommodates strain via grain boundary sliding accommodated by diffusion creep and limited dislocation creep.
- Dolomite leads to periodic embrittlement within the system, eventually allowing plastic flow of calcite.
- Grain boundary sliding is associated with CPO development.
- Monomineralic calcite bands accommodate more strain than bi-mineralic regions.

Supplementary Material – Microprobe Analysis

Microprobe analysis was performed on Dm25 and Dm75 deformed to high strain at 750°C (experiments P1527 and P1538). Figure S.1 is a map of all data points collected. Table S.1 gives xCa and xMg values at each point.

Figure S.1. Microprobe analysis maps. Data from Table S.1 is plotted as follows: yellow points represent Cc ($0.90<xCa<1.00$); green points represent Dm ($0.50<xCa<0.55$); red points represent Mg-enriched calcite ($0.55<xCa<0.90$). A. Microprobe analysis map for Dm25, P1527. B. Microprobe analysis map for Dm75, P1538.

Measurement Point	anion CO2	anion MgO	anion CaO	anion MnO	anion FeO	sum of x-site cation	xCa	xMg
'P1527_1_Scan3_1'	3.9768	0.1	1.9074	0.0027	0.0015	2.0116	0.9482	0.0497
'P1527_1_Scan3_2'	4.0527	0.4492	1.5184	0.0005	0.0056	1.9737	0.7693	0.2276
'P1527_1_Scan3_3'	4.0919	0.9298	1.0071	0.0012	0.0159	1.954	0.5154	0.4758
'P1527_1_Scan3_4'	4.0552	0.9527	1.0045	0.0013	0.0139	1.9724	0.5093	0.483
'P1527_1_Scan3_5'	4.048	0.0934	1.8816	0	0.001	1.976	0.9522	0.0472
'P1527_1_Scan3_6'	4.0326	0.1243	1.8564	0	0.0031	1.9837	0.9358	0.0627
'P1527_1_Scan3_7'	3.9979	0.1025	1.8959	0.0007	0.002	2.001	0.9474	0.0512
'P1527_1_Scan3_8'	4.0148	0.5163	1.4735	0.0002	0.0026	1.9926	0.7395	0.2591
'P1527_1_Scan3_9'	4.0552	0.0909	1.8771	0.002	0.0023	1.9724	0.9517	0.0461
'P1527_1_Scan3_10'	4.003	0.16	1.8335	0.0007	0.0043	1.9985	0.9174	0.0801
'P1527_1_Scan3_11'	4.0707	0.1161	1.8472	0	0.0013	1.9646	0.9402	0.0591
'P1527_1_Scan3_12'	3.9834	0.666	1.3355	0.0004	0.0064	2.0083	0.665	0.3316
'P1527_1_Scan3_13'	4.0165	0.5344	1.4495	0	0.0078	1.9917	0.7277	0.2683
'P1527_1_Scan3_14'	4.0305	0.9482	1.0176	0.0014	0.0175	1.9848	0.5127	0.4777
'P1527_1_Scan3_15'	4.04	0.9505	1.0105	0	0.019	1.98	0.5103	0.4801
'P1527_1_Scan3_16'	4.0309	0.121	1.8537	0	0.0099	1.9845	0.9341	0.0609
'P1527_1_Scan3_17'	4.0154	0.1114	1.8787	0.0005	0.0018	1.9923	0.943	0.0559
'P1527_1_Scan3_18'	4.1112	0.8974	1.0354	0.0008	0.0108	1.9444	0.5325	0.4615
'P1527_1_Scan3_19'	4.058	0.087	1.8828	0.0001	0.0011	1.971	0.9553	0.0442
'P1527_1_Scan3_20'	4.0394	0.7412	1.2265	0.0017	0.0109	1.9803	0.6193	0.3743
'P1527_1_Scan3_21'	4.0517	0.9514	1.0116	0.0014	0.0098	1.9742	0.5124	0.4819
'P1527_1_Scan3_22'	4.0916	0.1267	1.8251	0	0.0024	1.9542	0.9339	0.0648
'P1527_1_Scan3_23'	4.0508	0.0924	1.8812	0	0.001	1.9746	0.9527	0.0468
'P1527_1_Scan3_24'	4.0139	0.0698	1.9231	0.0001	0	1.9931	0.9649	0.035
'P1527_1_Scan3_25'	4.0043	0.0768	1.9209	0	0.0001	1.9978	0.9615	0.0385
'P1527_1_Scan3_26'	4.1012	0.9245	1.0035	0.0014	0.02	1.9494	0.5148	0.4742
'P1527_1_Scan3_27'	4.0163	0.9699	1.0104	0	0.0116	1.9919	0.5073	0.4869
'P1527_1_Scan3_28'	4.0299	0.1447	1.8372	0.0002	0.003	1.9851	0.9255	0.0729
'P1527_1_Scan3_29'	4.0392	0.8591	1.1071	0.0002	0.0141	1.9804	0.559	0.4338
'P1527_1_Scan3_30'	4.0826	0.0943	1.8626	0.0004	0.0015	1.9587	0.9509	0.0481
'P1527_1_Scan3_31'	4.0299	0.0824	1.9027	0	0	1.9851	0.9585	0.0415
'P1538_1_Scan4_1'	4.0297	0.9638	1.0036	0.0004	0.0174	1.9851	0.5056	0.4855
'P1538_1_Scan4_2'	4.0541	0.8177	1.1431	0.0002	0.012	1.9729	0.5794	0.4144
'P1538_1_Scan4_3'	4.0866	0.5664	1.3755	0.0014	0.0135	1.9567	0.703	0.2894
'P1538_1_Scan4_4'	4.052	0.9458	1.0066	0.0027	0.0189	1.974	0.5099	0.4791
'P1538_1_Scan4_5'	5.4704	1.0689	0.1651	0	0.0308	1.2648	0.1305	0.8451
'P1538_1_Scan4_6'	4.0593	0.8242	1.1338	0.0004	0.012	1.9704	0.5754	0.4183
'P1538_1_Scan4_7'	4.0453	0.4146	1.5548	0.0017	0.0064	1.9774	0.7863	0.2097
'P1538_1_Scan4_8'	5.3765	1.0137	0.2661	0	0.0319	1.3117	0.2029	0.7728
'P1538_1_Scan4_9'	4.0208	0.244	1.7439	0	0.0017	1.9896	0.8765	0.1226

Measurement Point	anion CO2	anion MgO	anion CaO	anion MnO	anion FeO	sum of x-site cation	xCa	xMg
'P1538_1_Scan4_10'	4.0303	0.2526	1.7291	0	0.0031	1.9848	0.8712	0.1273
'P1538_1_Scan4_11'	3.9954	0.6116	1.3775	0	0.0132	2.0023	0.688	0.3054
'P1538_1_Scan4_12'	4.005	0.954	1.0225	0	0.0209	1.9975	0.5119	0.4776
'P1538_1_Scan4_13'	4.0703	0.3188	1.6397	0.0003	0.0061	1.9649	0.8345	0.1623
'P1538_1_Scan4_14'	3.9921	0.2485	1.7506	0	0.0049	2.004	0.8736	0.124
'P1538_1_Scan4_15'	5.3297	1	0.3035	0.0004	0.0313	1.3351	0.2273	0.749
'P1538_1_Scan4_16'	4.0275	0.2997	1.6831	0.0004	0.0031	1.9863	0.8474	0.1509
'P1538_1_Scan4_17'	4.0487	0.2886	1.683	0.0001	0.004	1.9757	0.8519	0.1461
'P1538_1_Scan4_18'	4.0191	0.8969	1.0764	0.0023	0.0149	1.9905	0.5408	0.4506
'P1538_1_Scan4_19'	4.0512	0.2244	1.744	0	0.006	1.9744	0.8833	0.1136
'P1538_1_Scan4_20'	4.0398	0.2275	1.7464	0	0.0062	1.9801	0.882	0.1149
'P1538_1_Scan4_21'	4.0644	0.9409	1.0083	0.0006	0.018	1.9678	0.5124	0.4781
'P1538_1_Scan4_22'	4.0083	0.9745	1.0127	0	0.0087	1.9959	0.5074	0.4882
'P1538_1_Scan4_23'	4.0366	0.8325	1.1393	0.0012	0.0086	1.9817	0.5749	0.4201
'P1538_1_Scan4_24'	3.9877	0.5287	1.4693	0.0016	0.0066	2.0061	0.7324	0.2635
'P1538_1_Scan4_25'	4.051	0.3577	1.611	0	0.0058	1.9745	0.8159	0.1812
'P1538_1_Scan4_26'	4.0422	0.958	1.0063	0.0014	0.0132	1.9789	0.5085	0.4841
'P1538_1_Scan4_27'	4.0321	0.9484	1.0224	0.0005	0.0126	1.9839	0.5153	0.478
'P1538_1_Scan4_28'	4.0206	0.3519	1.6311	0.0003	0.0065	1.9897	0.8198	0.1768
'P1538_1_Scan4_29'	4.0119	0.2797	1.7101	0	0.0042	1.994	0.8576	0.1403
'P1538_1_Scan4_30'	4.0343	0.3951	1.5802	0.0005	0.0071	1.9829	0.7969	0.1992
'P1538_1_Scan4_31'	4.0021	0.5661	1.4204	0	0.0124	1.9989	0.7106	0.2832
'P1538_1_Scan4_32'	4.0717	0.8993	1.0524	0	0.0125	1.9641	0.5358	0.4578
'P1538_1_Scan4_33'	4.0094	0.306	1.6804	0.0011	0.0077	1.9953	0.8422	0.1534
'P1538_1_Scan4_35'	4.063	0.9209	1.0279	0.0002	0.0195	1.9685	0.5222	0.4678
'P1538_1_Scan4_36'	4.0375	0.2436	1.7313	0.0002	0.0061	1.9812	0.8739	0.1229
'P1538_1_Scan4_37'	4.0097	0.2306	1.7608	0.0015	0.0022	1.9951	0.8826	0.1156
'P1538_1_Scan4_38'	3.9981	0.9458	1.0373	0.0004	0.0175	2.001	0.5184	0.4727
'P1538_1_Scan4_39'	4.006	0.797	1.1846	0.0008	0.0146	1.997	0.5932	0.3991
'P1538_1_Scan4_40'	3.9713	0.9674	1.0289	0.0019	0.0162	2.0144	0.5108	0.4803
'P1538_1_Scan4_41'	3.9748	0.9435	1.0524	0.0003	0.0165	2.0126	0.5229	0.4688
'P1538_1_Scan4_42'	4.0177	0.2656	1.7218	0	0.0038	1.9912	0.8647	0.1334
'P1538_1_Scan4_43'	4.0178	0.9636	1.0125	0.0008	0.0143	1.9911	0.5085	0.4839
'P1538_1_Scan4_44'	4.012	0.9644	1.0157	0.0008	0.0131	1.994	0.5094	0.4836
'P1538_1_Scan4_45'	4.0054	0.9189	1.0637	0.0012	0.0136	1.9973	0.5326	0.4601
'P1538_1_Scan4_46'	4.0048	0.9705	1.0132	0.0006	0.0133	1.9976	0.5072	0.4858
'P1538_1_Scan4_47'	4.0462	0.9375	1.0264	0.0017	0.0113	1.9769	0.5192	0.4742
'P1538_1_Scan4_48'	3.9847	0.9823	1.01	0	0.0154	2.0077	0.5031	0.4893
'P1538_1_Scan4_49'	4.0671	0.2927	1.6676	0	0.0062	1.9665	0.848	0.1488
'P1538_1_Scan4_50'	4.0803	0.9191	1.0234	0.0009	0.0165	1.9599	0.5222	0.469

Measurement Point	anion CO2	anion MgO	anion CaO	anion MnO	anion FeO	sum of x-site cation	xCa	xMg
'P1538_1_Scan4_51'	3.9947	0.9127	1.0772	0.0002	0.0125	2.0027	0.5379	0.4558
'P1538_1_Scan4_52'	4.0099	0.2625	1.7285	0	0.004	1.9951	0.8664	0.1316
'P1538_1_Scan4_53'	4.0202	0.9551	1.018	0.0018	0.015	1.9899	0.5116	0.48
'P1538_1_Scan4_54'	4.026	0.7788	1.196	0.0005	0.0116	1.987	0.6019	0.3919
'P1538_1_Scan4_55'	4.0276	0.2161	1.7636	0.0006	0.0059	1.9862	0.8879	0.1088
'P1538_1_Scan4_56'	3.9652	0.7217	1.2812	0.0015	0.013	2.0174	0.6351	0.3577
'P1538_1_Scan4_57'	4.0506	0.2421	1.7277	0	0.0049	1.9747	0.8749	0.1226

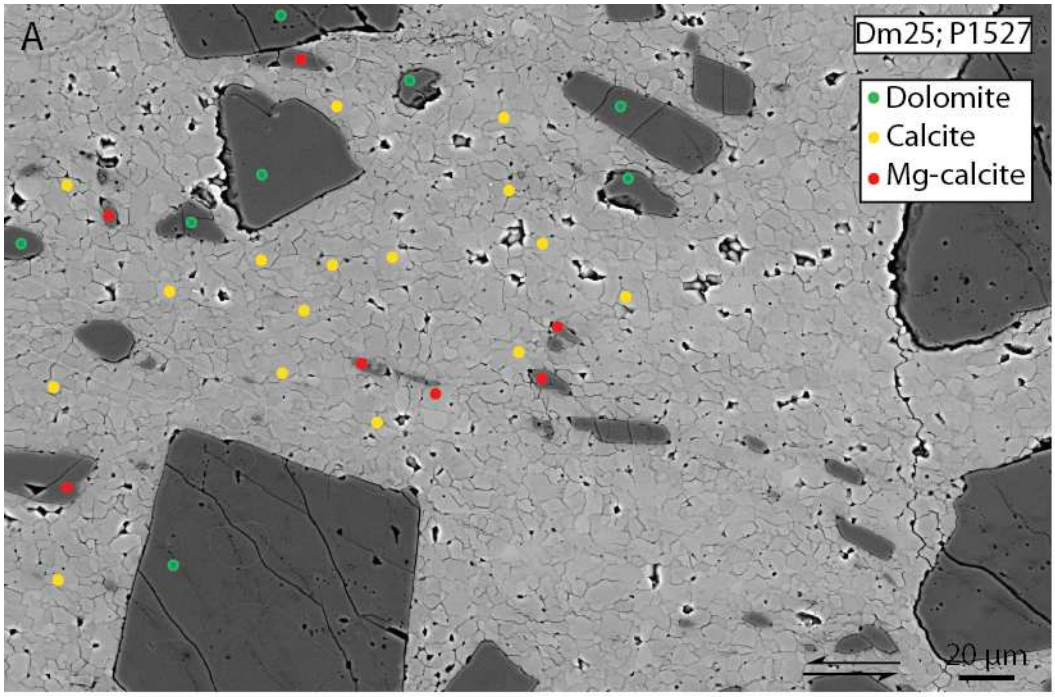
A
Dm25; P1527
Dolomite
Calcite
Mg-calcite
20 µm

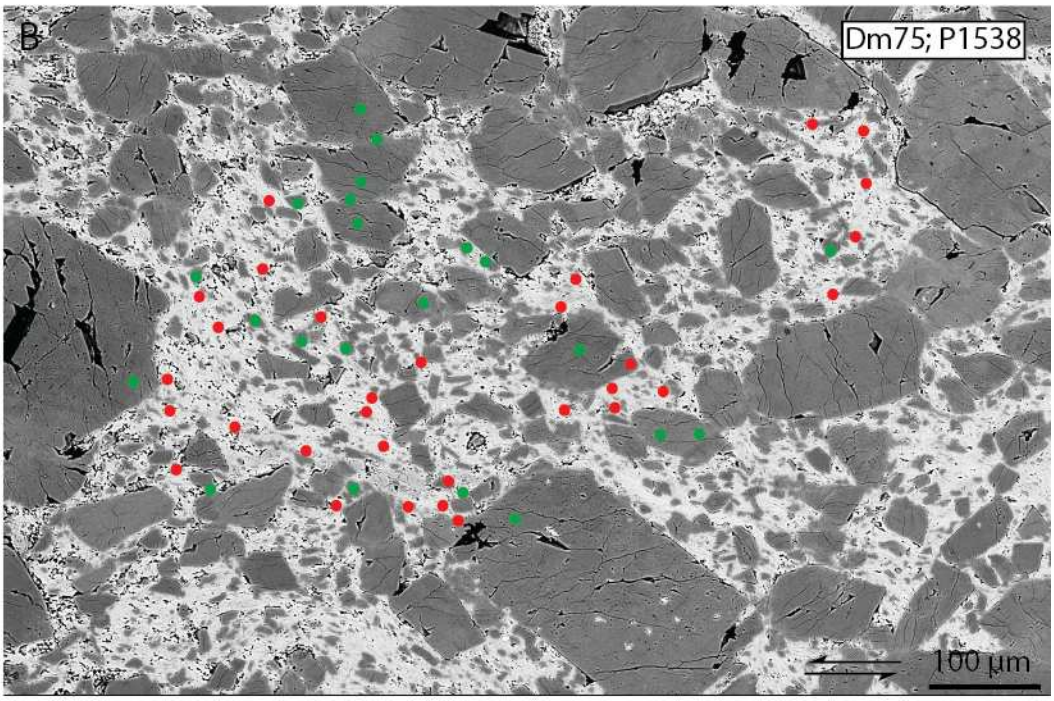
B
Dm75; P1538
100 µm